J. Fluid Mech. (2003), *vol.* 485, *pp.* 33–66. © 2003 Cambridge University Press
DOI: 10.1017/S0022112003004269 Printed in the United Kingdom

Space–time development of the onset of a shallow-water vortex

By J.-C. LIN, M. OZGOREN AND D. ROCKWELL

Department of Mechanical Engineering and Mechanics, 354 Packard Laboratory,
19 Memorial Drive West, Lehigh University, Bethlehem, PA 18015, USA

(Received 2 January 2002 and in revised form 2 January 2003)

An impulsively started jet in shallow water gives rise to vortices having a characteristic diameter larger than the water depth. A technique of high-image-density particle image velocimetry allows characterization of the space–time development of the instantaneous flow patterns along planes representing the quasi-two-dimensional and three-dimensional vortex structure. The quasi-two-dimensional patterns exhibit different categories of vortex development and interaction, depending upon the depth of the shallow water layer. Despite these distinctions, the variations of normalized vortex position, diameter, and circulation, as well as peak vorticity within the vortex, are very similar for sufficiently small water depth.

These quasi-two-dimensional patterns are, in turn, related to specific forms of three-dimensional flow structure, which is highly ordered. A prevalent feature is a vortex orthogonal to, and just ahead of, the primary, quasi-two-dimensional vortex. Its streamline topology, on a plane parallel to the axis of the quasi-two-dimensional vortex, exhibits a separation bubble with a well-defined separatix at the bottom (bed) surface. Moreover, its vorticity can exceed that of the quasi-two-dimensional pattern by a factor of two. This feature is consistent for all values of water depth. When the depth becomes sufficiently large, however, the three-dimensional vortex pattern involves an array of vorticity concentrations, which extends across the entire depth of the water.

On a plane very close to the bottom surface (bed), global instantaneous distributions of velocity and vorticity exhibit large gradients; they are associated with small-scale vorticity concentrations characteristic of rapid transition. The corresponding streamline topology of the averaged flow close to the bed, however, exhibits a stable focus and is a direct indicator of the topology well above the bed.

1. Introduction

1.1. *Overview of free-shear flows in shallow water*

Free-shear flows lead to vortex generation in shallow water, whereby the characteristic diameter of the vortex is larger than the water depth. This class of vortices occurs in a wide variety of hydraulic, environmental and geophysical flows, including flows in the following categories: flow channels having spanwise variations of either depth or bed friction coefficient; the merging of two rivers; the entrance to a harbour; a sudden expansion of a channel geometry; discharge into a river or lake; and an evacuation region of a coastal lagoon. In addition, flow past large obstacles, such as islands, stranded oil tankers, and large-scale bridge piers can also generate vortices. The onset and development of shallow-water vortex systems strongly influences the diffusion of pollutants, thermal mixing, and the erosion of the bed (bottom surface). In recent years, considerable insight has been provided into the onset and development of shallow-water vortices generated in basic classes of shear flow, namely mixing layers, wakes, and jets.

Mixing Layers Alavian & Chu (1985) investigated the shallow turbulent flow over a compound channel and addressed the stability characteristics of the shear flow; in addition, they experimentally determined the mean velocity distribution and turbulent viscosity coefficient. Chen & Jirka (1986) characterized the linear stability of a shallow turbulent mixing layer. Chu & Babarutsi (1988) considered the case of a shallow mixing layer and determined the critical value of the bed friction number for the instability. Chu, Wu & Khayat (1991) investigated the generation of transverse shear in a shallow open channel flow by spanwise variations of either water depth or bed friction coefficient, and determined the critical value of the bed friction number for the shallow mixing layer. Uijttewall & Tucker (1988) considered in detail the turbulent statistics, including correlations and spectra of the large-scale structures in a shallow mixing layer.

When two streams of unequal depth merge together, they form a complex, three-dimensional mixing layer at the confluence, as revealed by Best & Roy (1991). Further details of the turbulence statistics of this type of configuration are provided by Biron, Roy & Best (1996). They found that the flow pattern exhibits fluid upwelling in the vertical direction and altered mixing in the separated shear layer.

Wakes Shallow-water vortex systems in wakes have been generated by bluff obstacles and observed in both field and laboratory environments. Ingram & Chu (1987) considered both full-scale and scaled models of bluff body wakes and addressed the roles of transverse shear and bed friction effects. Chen & Jirka (1995) experimentally characterized shallow wakes from bluff bodies and defined three basic classes of wake patterns. Grubisic, Smith & Schar (1995) addressed the amplification of absolutely unstable disturbances in the near wake for approximations to the near-wake velocity profile. Chen & Jirka (1997) theoretically determined the conditions for existence of convective and absolute instabilities of the near-wake vortex system of a cylinder and emphasized the crucial role of bed friction. Lloyd & Stansby (1997) performed experimental and numerical studies of the vortex formation from model conical islands in shallow water and defined regimes of possible wake patterns. Akilli & Rockwell (2002) characterized the structure of vortex formation in the near wake of a cylinder as a function of elevation above the bed, in terms of patterns of vorticity and streamline topology. The effects of ordered roughness elements along the bed were characterized by Kahraman, Sahin & Rockwell (2002); their influence on large-scale vortex formation extends well above the surface of the bed.

The nature of the near-wake instability, and its effect on downstream regions of the flow, will, of course, have consequences for concentration fields, as well as length and velocity scales of the wake. These features have been addressed by Balachandar, Chu & Zhang (1997) and Balachandra, Tachie & Chu (1999), who performed concentration measurements. Furthermore, Balachandar, Ramachandran & Tachie (2000) examined the turbulence statistics of the near-wake region at low Reynolds number, and Tachie & Balachandar (2001) characterized the nature of wakes on smooth and rough surfaces.

Jets Giger, Dracos & Jirka (1991) and Dracos, Giger & Jirka (1992) assessed both the turbulent characteristics and entrainment features of jets in shallow water. Moreover, they determined the importance of water depth as an appropriate length scale for normalization. Chen & Jirka (1993, 1998) focused on defining the mixing characteristics of shallow-water jets using a laser-induced fluorescence technique. In a subsequent study, Chen & Jirka (1999) addressed theoretically the instability of the shallow jet and described the possibility of 'relaminarization', i.e. stabilization, of a shallow jet.

All of the foregoing classes of investigation have provided valuable insight into the central features of vortex systems in shallow water, in particular in the intermediate and far regions of mixing layers and jets, and in the near region of wakes. Of particular interest in the present investigation is the structure of a shallow-water vortex immediately at its onset, that is, in the very near region. To this end, it is appropriate to address previous related investigations in the near regions of basic shear flows. In selecting these previous studies, emphasis is given to those that incorporate descriptions of the flow physics that are likely to be relevant to the present study.

1.2. *Near-region of free-shear flows in shallow water: physical aspects*

The near-field development of low-aspect-ratio jets, bounded by a solid wall, rather than a free surface, was first investigated in detail by Foss & Jones (1968) and Holdemann & Foss (1975). They characterized the three-dimensional features of a jet having a nozzle height to width ratio $H/B = 4$, and clearly demonstrated the existence of streamwise vorticity associated with secondary currents in the jet. The consequence of this secondary motion was a deficit of momentum flux along the midplane of the jet. Rockwell (1977) visualized the three-dimensional development of the jet vortices in a similar configuration, and showed the three-dimensional deformation of the nominally two-dimensional vortices in the jet shear layer. The physical findings of these investigations are, of course, related to the turbulence statistics of the developing jet.

Dracos *et al.* (1992) effectively scaled the root-mean-square of the streamwise velocity fluctuation along the jet axis for varying ratios of jet height to nozzle width H/B and incorporated the data of Holdemann & Foss (1975). Based on this scaling, they ascertained that the effect of the secondary motion was maximum at a distance of approximately $x/H = 6$ and, furthermore, at larger streamwise distances, a plateau of the scaled velocity fluctuation was attained. In all of these investigations, the values of nozzle height to width ratio ranged from $H/B = 4$ to 36 and, for the purposes of our present considerations, do not necessarily represent a shallow configuration in the very near region. Nevertheless, the physical aspects are generic and provide a suitable basis for guiding interpretation of the current observations.

Irrespective of whether the shallow shear layer occurs in the form of a jet, wake or mixing layer, it can lead to the generation of a vortex or a system of vortices. An important physical feature of a line vortex oriented orthogonal to and translating along a continuous wall is the occurrence of axial flow along the core of the vortex. This flow is directed from the wall towards the free stream. Kurosaka *et al.* (1988) injected dye at a sidewall and observed axial flow in the vortices formed in a free-shear flow and in a Kármán vortex street. Akilli & Rockwell (2002) have also characterized the onset of axial flow due to the formation of a Kármán vortex street. The early investigation of Koochesfahani (1989) clearly demonstrated an axial flow mechanism for an experiment where dye was injected at the sidewalls of a pitching airfoil arrangement. This type of controlled excitation provided remarkable patterns showing the evolution of the axial flow with the generation of successive vortices. In a later investigation, Cohn & Koochesfahani (1993) found that such axial flow could occur in a line vortex, even when a no-slip condition at a wall is imposed over a limited spatial region that is comparable to the core diameter of the vortex. They also found that such axial flow is possible without a no-slip condition, provided that a region of spanwise shear exists.

A related configuration involves a columnar vortex, whose axis is maintained orthogonal to the leading edge of a thin plate, which it impinges upon, and is cut during its translation along the plate. Krishnamoorthy & Marshall (1998) and Marshall & Krishnamoorthy (1997) performed numerical simulation and qualitative dye visualization of the complex, three-dimensional vortical patterns induced by the vortex interaction with the plate boundary layer. Most relevant to our present considerations is the scenario of Marshall & Krishnamoorthy (1997), for which the vortex–plate cutting process involves an initially prescribed vortex with a defined magnitude of flow along its axis. Sectional cuts of the numerically computed azimuthal vorticity field show a series of vortex rings of alternating sign along the axis of the vortex. These vortex rings were represented by patterns of azimuthal vorticity on a plane extending over the trailing half of the vortex.

For all of the foregoing situations of a vortex orthogonal to a surface, study of the relationship between the surface flow pattern and the flow field above it can benefit from the application of topological concepts. Perry & Chong (1986) employ concepts of critical point theory, along with series expansion solutions of the Navier–Stokes and continuity equations to determine the relationship between the three-dimensional flow pattern above a surface and the pattern along the surface. One class of solutions leads to an upward flow, which emanates from the centre of a swirl streamline pattern at the surface. This upward flow is through the centre of a helical streamline pattern. This general type of framework is appropriate for classification of the near-surface flow patterns of interest in the present investigation.

All of the foregoing investigations reveal physical elements that are expected to be present in the formation region of a vortex in shallow water. They will be interpreted in the context of the present observations.

1.3. *Issues and objectives*

Consideration of previous investigations, as described in the foregoing, allows the identification of the following unresolved issues related to the very near region of vortex formation in shallow water.

(1) The detailed physics of the initially formed vortex in shallow water has not been addressed. For the particular case of a jet, very low values of aspect ratio, defined as the jet height H to its width B, down to $H/B < 1$, are of interest.

(2) An understanding of the physics of near-field vortex development in shallow water has not been represented by global patterns of velocity, vorticity and streamline topology. This approach would allow the surface (bed) flow patterns to be related to the flow away from the surface, and provide a basis for understanding bed loading associated with the initial stages of erosion and sediment transport.

(3) The quasi-two-dimensional evolution of the initially formed vortex as a function of water depth is unclear. It is expected that the overall shape of the vortex will be a function of both water depth and streamwise distance. In addition, in view of the shallow nature of the vortex and the expected occurrence of three-dimensionality, the form of the vorticity distribution across the quasi-two-dimensional vortex may not be a smooth and continuous one. Rather, highly concentrated regions of vorticity may be embedded within the vortex core. This type of vorticity variation would contrast with that occurring for the well-known ring vortex or a typical vortex in a mixing layer of large spanwise extent. Furthermore, the rate of decay of the vorticity

in the shallow vortex may be a function of dimensionless water depth, but remains unclarified. Finally, the question arises as to whether universal topological features of streamline patterns are attainable for the quasi-two-dimensional vortex, irrespective of water depth.

(4) The three-dimensional structure of the initially formed shallow vortex has not been addressed. On the basis of the foregoing investigations, one expects the occurrence of axial flow along the core of the vortex in a direction from the wall towards the free-surface. To date, this axial flow has been addressed primarily with dye visualization marker and pointwise velocity measurements. A global imaging technique provides the potential for interpreting this axial flow mechanism and, more importantly, whether it is accompanied by patterns of vorticity whose axes are orthogonal to the primary, quasi-two-dimensional vortex. In the case where the water becomes sufficiently shallow relative to the characteristic diameter of the vortex, one expects either suppression or radical alteration of the three-dimensional mechanisms.

(5) The bed (bottom surface) will be influenced by the quasi-two-dimensional and three-dimensional features of the vortex structure described in the foregoing, but this relationship is unclear. The patterns of vorticity and the streamline topology in a plane very close to the bed are expected to exhibit a number of unique features. In a general sense, the degree to which the topology adjacent to the bed is a footprint of the quasi-two-dimensional topology above it is an important concept. Although the averaged topology of, for example, streamlines immediately adjacent to a wall has been interpreted for other types of flow configurations, it has not been addressed for shallow-water vortex systems. More importantly the sequence of instantaneous topological states that gives rise to the averaged topology has not been defined.

The objectives of the present investigation are centred on the resolution of the aforementioned issues. A technique of high-image-density particle image velocimetry is employed to characterize the quasi-two-dimensional and three-dimensional features of a shallow-water vortex system generated in a highly controlled and repeatable manner.

2. Experimental system and techniques

Experiments were performed in a custom-designed shallow-water table, which is illustrated in the schematic of figure 1. It was constructed of optical quality glass, which allowed access from the bottom and sides. The table had a width of $W_t =$ 914.4 mm, a length $L_t = 1524$ mm, and a height $H_t = 133.4$ mm. The height h_w of the shallow water was adjustable. Values of $h_w = 6.35$ mm to 25.4 mm were employed for the present studies.

The piston–nozzle arrangement is shown in the plan and side views of figures 1 and 2. It represents a shallow-water version of systems employed to generate vortex rings in free space (e.g. Gharib *et al.* 1998). The present system extended well above the height h_w of the shallow water. The length of the nozzle was $L_N = 211$ mm. The width of the nozzle was $W = 25.4$ mm and the piston moved with a velocity U_p. Details of the piston system are shown in figure 2. The length of the piston was $L_p =$ 50.8 mm, and its stroke was $S = 152.4$ mm. This value of U_p was abruptly attained after the onset of the piston motion (4 ms later) and maintained during the entire piston stroke. The piston stops at the location $L_s = 13$ mm before the tip of the nozzle exit. The motion of the piston was controlled by a high-resolution stepping motor, which was interfaced with a laboratory microcomputer. Preliminary experiments showed that a value of piston velocity $U_p = 50.8\,\mathrm{mm\,s^{-1}}$ provided optimum generation

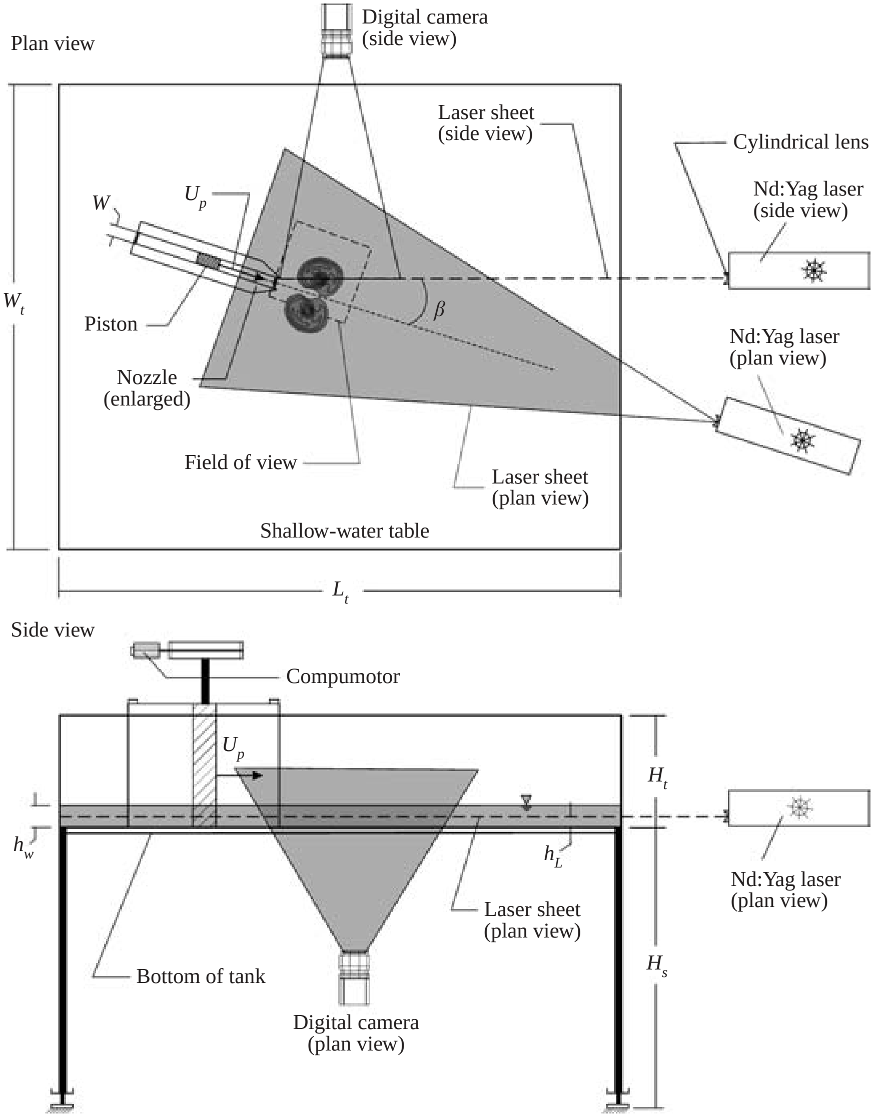

FIGURE 1. Overview of the shallow water table, piston–nozzle assembly for the generation of the vortex system, and the arrangement of the imaging system for characterizing the side and plan views of vortex development.

of large-scale vortices over a range of water depth, and this value was employed for all cases herein.

A major focus of the present investigation is to characterize the development of shallow vortices bounded by a solid (bottom) surface and a free surface. A cover plate could not be deployed at the elevation of the free surface, at locations within the nozzle; such a plate would have led to unacceptable generation of vorticity. As a consequence, small-amplitude distortion of the free surface is inevitable as a result of the start-up process of the piston motion. In all cases, this maximum deviation and elevation of the free surface was less than $0.03h_w^*$, where $h_w^* = h_w/W$ is dimensionless water depth. Nevertheless, significant variation with time of the shallow-water jet

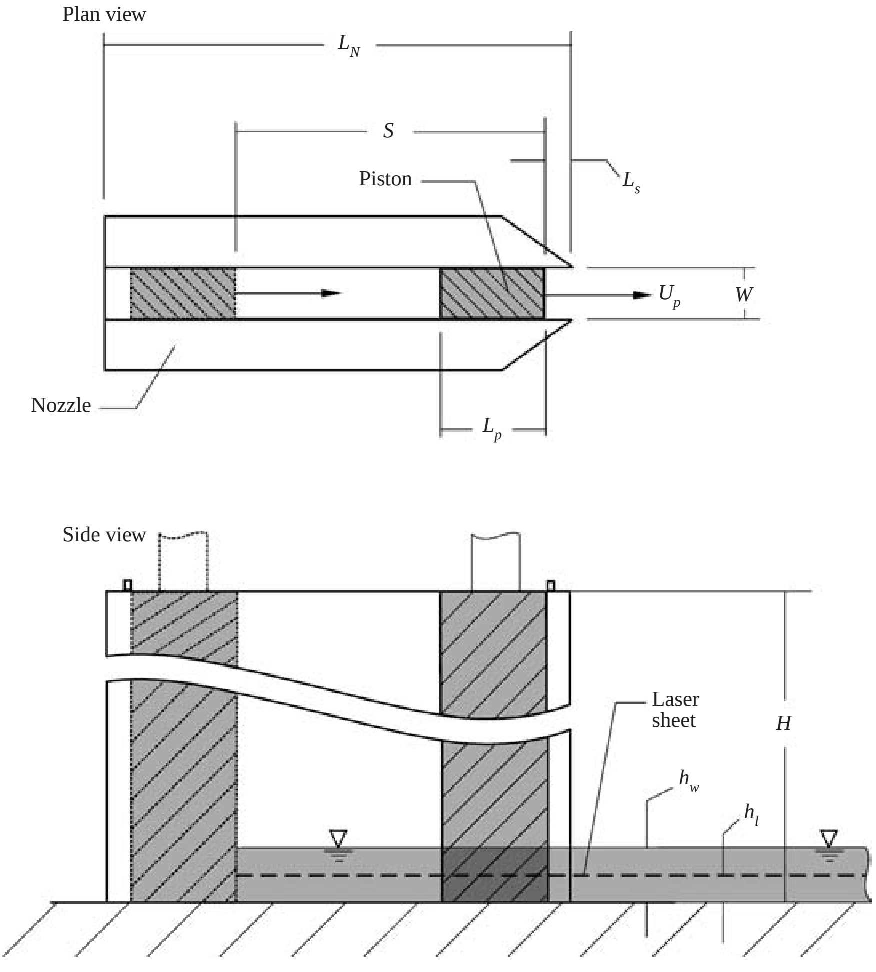

Figure 2. Schematic of nozzle–piston system for the controlled generation of vortices in shallow water.

at the nozzle exit arises from this wave-like motion. The consequence is to induce a delay of the onset of the nozzle exit velocity, relative to the piston motion. It will be demonstrated below that if this time delay t_s is properly accounted for in the definition of dimensionless time, then the major quantitative features of the vortex development, represented by vortex position, diameter, circulation, and peak vorticity, show the same general form for the two shallowest water depths considered herein, for which detailed three-dimensional analysis of the vortex structure was performed.

Figure 3(*a*) shows the first effective cycle of the velocity variation at the nozzle exit; this cycle is associated with generation of the initial, primary vortex, whose three-dimensional features are the primary focus of this investigation. As water depth h_w decreases, the time delay t_s between the onset of piston motion and the effective onset of the jet velocity U increases. The second effective cycle of the jet velocity at the nozzle exit is shown in figure 3(*b*). It was found that the second cycle did not influence the vortex development, which was of a generally similar form to that arising from the first cycle.

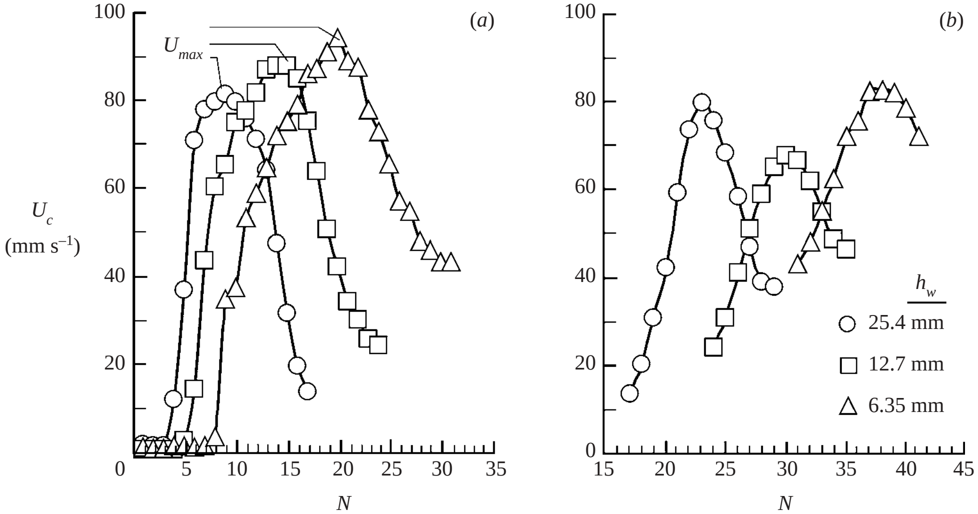

FIGURE 3. Variation of velocity U_c at the centreline ($y = 0$) of the nozzle exit. (a) The first effective cycle, (b) the second effective cycle.

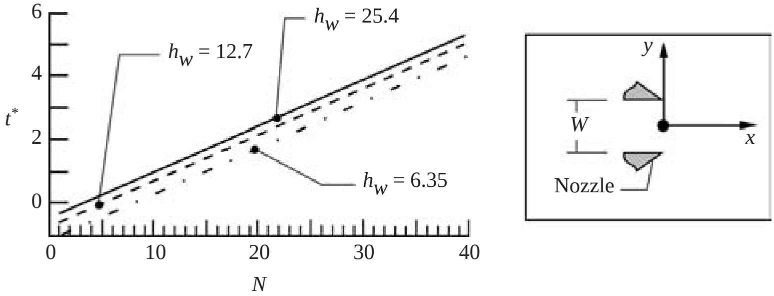

FIGURE 4. Relation between the dimensionless time t^* and the frame number N.

The relationship between time t and frame number N is $t = 0.0713\,(N - 1)$. Furthermore, it is possible to define a dimensionless time $t^* = (t - t_s)U_p/W$, in which U_p is the constant piston velocity and W is the nozzle width. The relationship between t^* and frame number N shown in figure 4 is $t^* = 0.142N - K$, in which $K = 0.428$, 0.713, and 1.14 for values of water depth $h_w = 25.4$, 12.7, and 6.35 mm, respectively.

The distribution of velocity across the nozzle exit will be influenced by viscous effects associated with the development of boundary layers along the nozzle wall. Figures 5(a), 5(b) and 5(c) show the development of the velocity profile at successive instants corresponding to $U_{max}/2$, $2U_{max}/3$, and U_{max}, in which U_{max} corresponds to the maximum value of velocity attained during the first cycle, represented by figure 3(a). For each value of water depth h_w, the value of U_{max} occurs at successively later times for decreasing water depth. At each instant, i.e. at $U_{max}/2$, at $2U_{max}/3$, and U_{max}, and at a given value of water depth h_w^*, the peak value of the velocity across the nozzle exit is designated as U_0 and serves as the normalization factor for the dimensionless distribution of velocity U/U_0. At U_{max}, $2U_{max}/3$ and $U_{max}/2$, the respective values of U_0 are $U_0 = 87$, 72 and 48.6 mm s^{-1} at $h_w = 25.4$ mm; $U_0 = 90$, 75 and 53.2 mm s^{-1} at $h_w = 12.7$ mm; and $U_0 = 95.5$, 82 and 65.3 mm s^{-1} at $h_w = 6.35$ mm. Using this normalization, it is evident that the general form of the velocity distribution is very

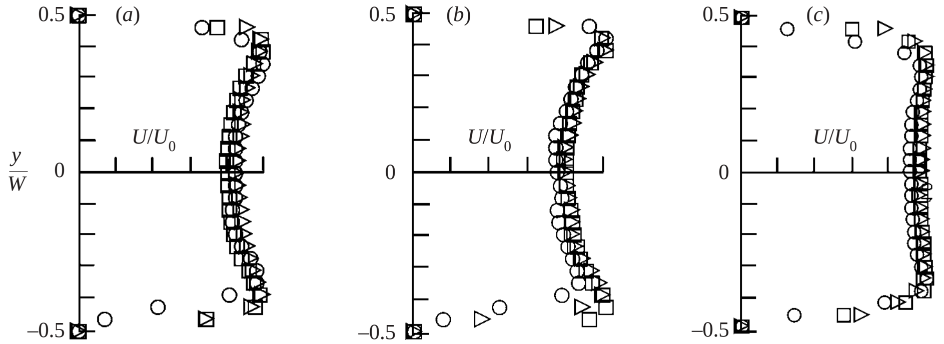

FIGURE 5. Normalized distributions of velocity across the nozzle exit: (*a*) at $\frac{1}{2}U_{max}$, (*b*) at $\frac{2}{3}U_{max}$, (*c*) at U_{max}.

similar at each successive instant for all values of water depth h_w^*. It is this portion of the jet velocity variation up to U_{max} that generates the major (primary) vortex, which is the focus of the three-dimensional assessments given in subsequent sections. Furthermore, it should be noted that the evolution with time of the shape of the velocity profile at the nozzle exit is very similar to that of Didden (1979) for the generation of vortex rings from a submerged axisymmetric nozzle.

For water depths of $h_w = 6.35$, 12.7 and 25.4 mm, the values of the Reynolds numbers based on maximum velocity U_0 and nozzle width W were $Re_w = 2158$, 2040 and 1971. Using water depth as the characteristic length, $Re_{h_w} = 538$, 1020 and 1971.

A technique of digital particle image velocimetry (DPIV) was employed to characterize the instantaneous quasi-two-dimensional and three-dimensional features of the flow structure. The water was seeded with 14 μm metallic coated particles. Two principal orientations of the laser sheet were employed. For the plan view, as defined in figure 1, the laser sheet was parallel to the bottom surface of the water table and located a distance h_L above the surface. For the side view, the laser sheet was oriented vertically and cut through the vortex system at an angle β with respect to the centreline of the nozzle. A 90 mJ Nd:Yag dual laser system was employed to generate double pulses, which, for the present experiment, had time delays ranging from $\Delta t = 3$ ms to 6 ms. A cylindrical lens system was employed to produce the laser sheet, which had a thickness of 1 mm.

The patterns of particle images were recorded on a CCD camera having a resolution of 1008 pixels × 1018 pixels. For the plan view, a value of magnification M = 1:15.3 was employed. This provided a field of view of 62.6 mm × 63.7 mm in the plane of the laser sheet. It is designated by the dashed lines in the plan view of figure 1. For the side view, the magnification was $M = 1{:}27$, yielding fields of view 35.6 mm × 5.8 mm and 35.6 mm × 12.1 mm. In all cases herein, where plan and side views are compared directly, the scales of the images were adjusted during post-processing such that the plan and side views have the same scale. Patterns of particle images were acquired at a rate of twenty-eight frames per second, thereby allowing fourteen frame pairs per second. A frame-to-frame cross-correlation technique was employed to determine the velocity fields. The effective size of the interrogation window was 32 pixels × 32 pixels. The interrogation area contained approximately 15 to 25 particle images. The effective grid size, in the plane of the laser sheet, for the plan and side views, was 1.062 mm × 1.062 mm and 0.602 mm× 0.602 mm respectively. In order to satisfy

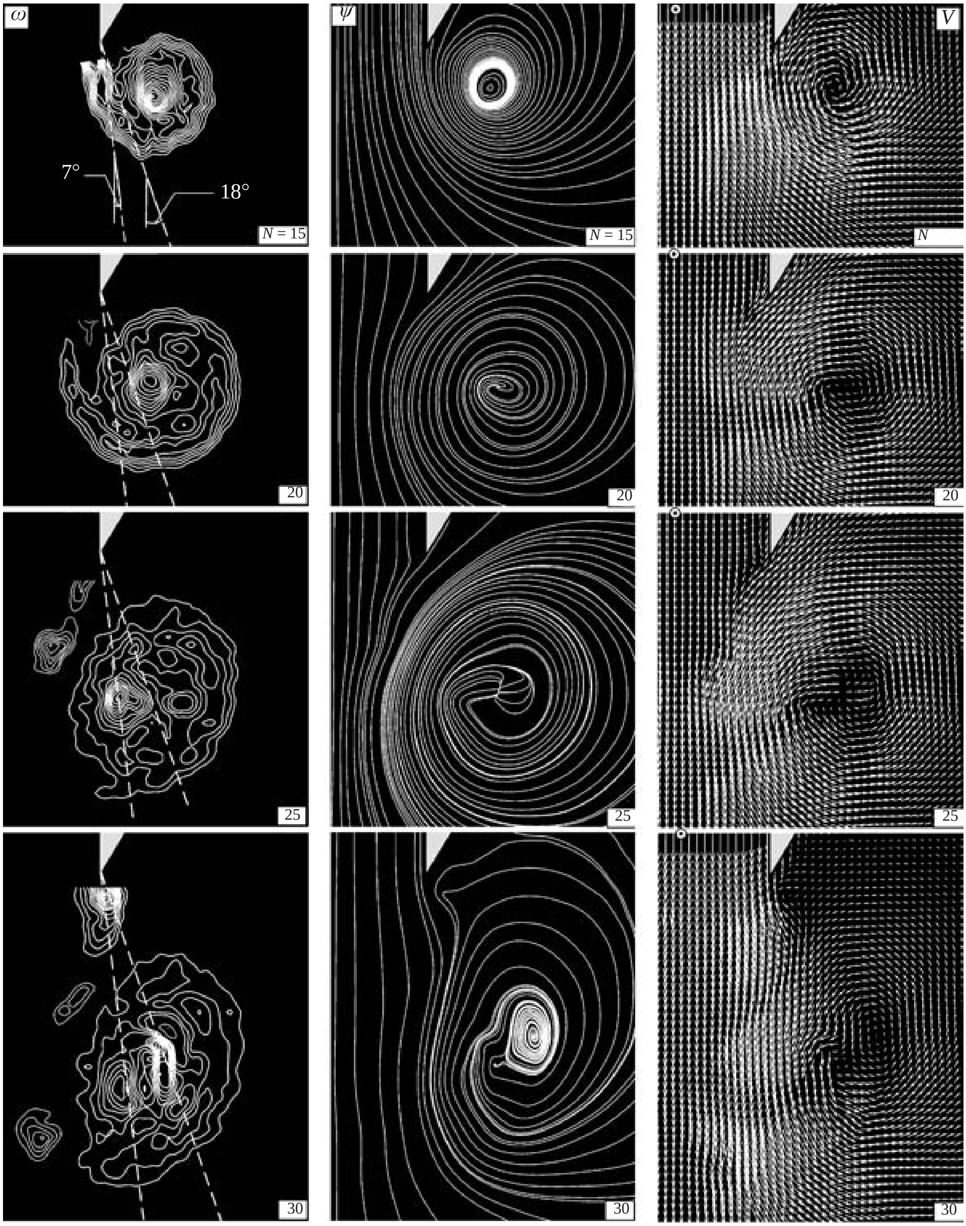

FIGURE 6. For caption see facing page.

the Nyquist criterion, an overlap of 50% was employed during the interrogation process. This procedure yielded approximately 3782 velocity vectors in the plan view. For the side view, 610 vectors were obtained for the dimensionless water depth $h_w^* = h_w/W = 0.25$, and 1342 vectors for $h_w^* = 0.5$. The factors that contribute to the uncertainty of velocity measured using the PIV technique are critically assessed by Adrian (1991), Raffel, Willert & Kompenhans (1998) and Westerweel (1993). The digital PIV (DPIV) approach employed herein is similar to that evaluated by Westerweel (1993); he concludes that an uncertainty in velocity of less than 2% is an

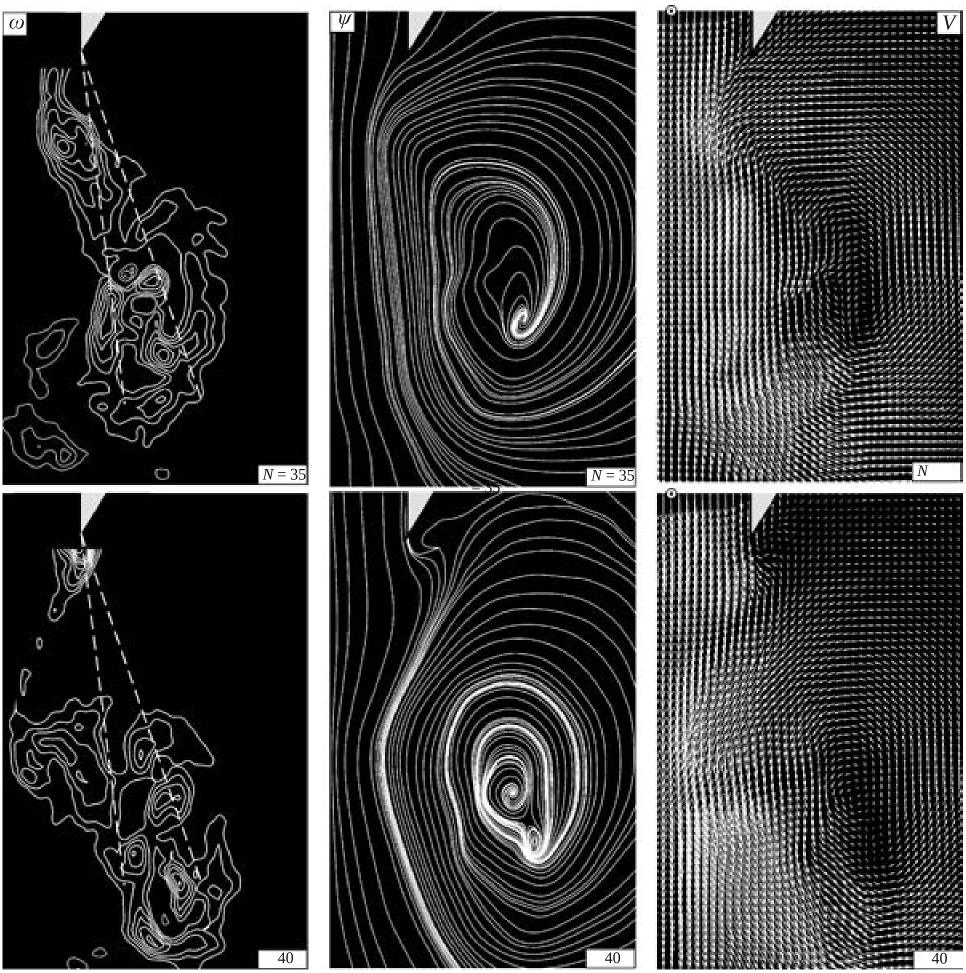

FIGURE 6. Plan views of patterns of instantaneous vorticity ω, streamlines ψ and velocity V corresponding to a laser sheet located at half-depth. Depth of water is $h_w^* = h_w/W = 0.5$ and laser sheet is located at a distance of $h_L^* = h_L/W = 0.25$ beneath the free surface. Minimum and incremental values of instantaneous vorticity ω are respectively $\omega_{min} = \pm 4$ and $\Delta\omega = 2\ \mathrm{s}^{-1}$. N represents the frame number of the image sequence. Dashed white lines correspond to orientations of vertical laser sheets employed for side views of vortex development. The white dot on the reference velocity vector represents values of velocity 89, 46, 32, 77, 48 and 79 mm s^{-1}, for images $N = 15$ to 40 respectively. The primary vortex is shown by thick white lines, and vorticity concentrations of opposite sense by thin white lines.

appropriate estimate. These patterns of velocity were employed, in turn, to construct instantaneous patterns of vorticity and the corresponding streamline topology. It was then possible to compare this instantaneous structure at successive times, due to the aforementioned cinema mode of image acquisition. For the image sequences shown herein, the timewise development is represented by the frame number N of the image.

3. Quasi-two-dimensional flow structure

Figure 6 shows the evolution of the vortex formed in the jet at a dimensionless water depth of $h_w^* = h_w/W = 0.5$. The laser sheet was located at a distance of

$h_L^* = h_L/W = 0.25$ from the bottom surface of the table, i.e. the bed. These patterns of figure 6 represent the plan view of the sectional cut of the vortex development. Contours of instantaneous vorticity (left-hand column), instantaneous streamline patterns (middle column) and instantaneous velocity vectors (right-hand column) are directly compared. In the image at the upper left of figure 2, white dashed lines are shown at angles of $\beta = 7°$ and 18°. These lines correspond to vertical cuts, which will be employed for side views of the vortex development.

At $N = 15$, the instantaneous structure of the vortex exhibits a region of highly concentrated vorticity near the centre of the vorticity pattern, and this high concentration persists at $N = 20$ and 25. At subsequent times, corresponding to $N = 30$, 35 and 40, several regions of highly concentrated vorticity become evident. It will be demonstrated that these regions of concentrated vorticity within the central portion of the vortex are associated with three-dimensional effects. Furthermore, in addition to the primary vortex, whose vorticity is represented by thick white lines, vorticity concentrations of opposite sense, represented by the thin white lines, are generated from the exterior surface of the nozzle. Their identity persists to relatively large times, e.g. a time corresponding to image $N = 35$. A further feature of the development of the pattern of vorticity is the overall shape of the outermost vorticity contour. It transforms from a nearly circular form at $N = 15$ and 20 to an elongated form at $N = 35$ and 40. Finally, the location of the highly concentrated region of vorticity within the vortex moves towards the left-hand boundary of the vorticity contours, as the flow develops in images $N = 15$ to 35. Patterns of instantaneous streamlines are shown in the middle column of figure 6. The corresponding patterns of velocity, shown in the right-hand column of figure 6, provide guidance for interpretation of the direction of the streamlines. At $N = 15$, they initially take the form of a limit cycle (thick white circle). Concentric closed streamlines are embedded within the limit cycle. This topology means that the central region of the vortex is two-dimensional. On the other hand, exterior to the limit cycle, the streamlines spiral outward. At a later time, corresponding to $N = 20$, the two-dimensional centre of the vortex no longer exists. Rather, the entire streamline pattern spirals in the outward direction, corresponding to an unstable focus at its centre. At a subsequent instant, represented by image $N = 25$, the general form of the streamline pattern is still an outward spiral, though its centre exhibits a nodal line. The general pattern of outward-spiralling streamlines, and thereby an unstable focus at the centre, generally persists at larger values of $N = 30$, 35 and 40.

4. Effect of water depth on quasi-two-dimensional vortex development

Figure 7(*a*) shows plan views of the instantaneous vortex structure as a function of dimensionless water depth $h_w^* = h_w/W$. As a reference, the middle column of images corresponds to the water depth $h_w^* = 0.5$, which was addressed in the previous section. At this water depth, as well as at the shallower and deeper water levels shown respectively in the left- and right-hand columns of images, the horizontal laser sheet was always located at mid-depth, that is, halfway between the free surface and the bottom surface of the water table. Viewing figure 7(*a*) as a whole, it is evident that the water depth has a pronounced influence on not only the general form of the vorticity concentrations, but also on the peak values of vorticity. For the shallowest water $h_w^* = 0.25$, shown in the left-hand column, the vorticity levels are rapidly attenuated with increasing time, i.e. with increasing values of N. Although a degree of attenuation occurs for the images at $h_w^* = 0.5$ shown in the middle column, pronounced, relatively high levels of vorticity concentrations still persist. Finally, for the deepest water $h_w^* = 1$ shown in the right-hand column, the overall form of the vorticity concentrations dramatically departs from that of cases corresponding to shallower water. Moreover, highly concentrated regions of vorticity persist even until $N = 40$.

The corresponding streamline patterns are shown in figure 7(*b*). They show, for the shallowest water level in the left-hand column, a consistent pattern of outward-spiralling streamlines, corresponding to an unstable focus at the centre of the vortex. This form of topology is remarkably consistent for the entire development of the vortex. Generally similar patterns of outward-spiralling streamlines are evident in the middle column of images of figure 7(*b*). At a relatively late time $N = 40$, however, two foci are indicated in the central portion of the vortex for the case $h_w^* = 0.5$. Finally, for the deepest water represented in the right-hand column of figure 7(*b*), limit-cycle patterns of streamlines are attainable. The pattern at $N = 20$ suggests the onset of a limit cycle, and the subsequent images at $N = 30$, 35 and 40 clearly depict a closed (limit-cycle) streamline.

5. Quasi-two-dimensional vortex development: quantitative evaluation

It is evident from the images shown in figures 6 and 7 that the quasi-two-dimensional or sectional structure of the vortex exhibits patterns of velocity, vorticity and streamline topology that are influenced by three-dimensional effects; this is the focus of the present investigation, and will be addressed in detail. At this point, however, some insight is gained by examining overall features of the vortex development, in analogy with the extensively investigated cases of two-dimensional (axisymmetric) vortices. At each value of water depth h_w^*, cinema sequences of the instantaneous patterns of velocity were determined for a total of 40 images. These velocity patterns were evaluated to yield instantaneous distributions of vorticity. Using this general approach, it was possible to determine the patterns of representative vortex position X_v, Y_v, vortex diameter D_v, circulation Γ, and peak vorticity ω_p.

Figure 8 shows plots of the streamwise X_v and transverse Y_v locations of the peak value of vorticity ω_p within each vorticity distribution at successive instants of time. Figures 8(*a*) and 8(*b*) show values of vortex position X_v and Y_v normalized by the nozzle width W. Dimensionless time is $t^* = (t - t_s)U_p/W$, in which t_s is the delay time between the onset of piston motion and the onset of a finite velocity at the nozzle exit, as indicated in figure 8. Using a best fit through each of the data sets for each value of h_w^*, the constant velocity of the vortex is 13.05, 19.5 and 17.1 $\mathrm{mm\,s^{-1}}$ respectively for $h_w^* = 1.0$, 0.5 and 0.25. As will be described below, the two shallowest water depths $h_w^* = 0.25$ and 0.5 are the focus of this investigation.

Furthermore, the characteristic vortex diameter D_v normalized by nozzle width W is given in figure 8(*c*). The value of D_v was determined at each instant by measurement of the diameter of the lowest-level contour of vorticity in, for example, the images of figures 6 and 7. When the pattern of vorticity became sufficiently distorted that it exhibited an approximately elliptical, as opposed to circular, shape, the average of the major and minor axes of the vortex was used to represent the diameter D_v. Again, values of dimensionless water depth $h_w^* = 0.25$ and 0.5 are of primary interest in subsequent sections, and these plots of D_v/W exhibit a similar form. In contrast, due to apparently stronger three-dimensional effects, substantial differences for depth $h_w^* = 1.0$ are evident.

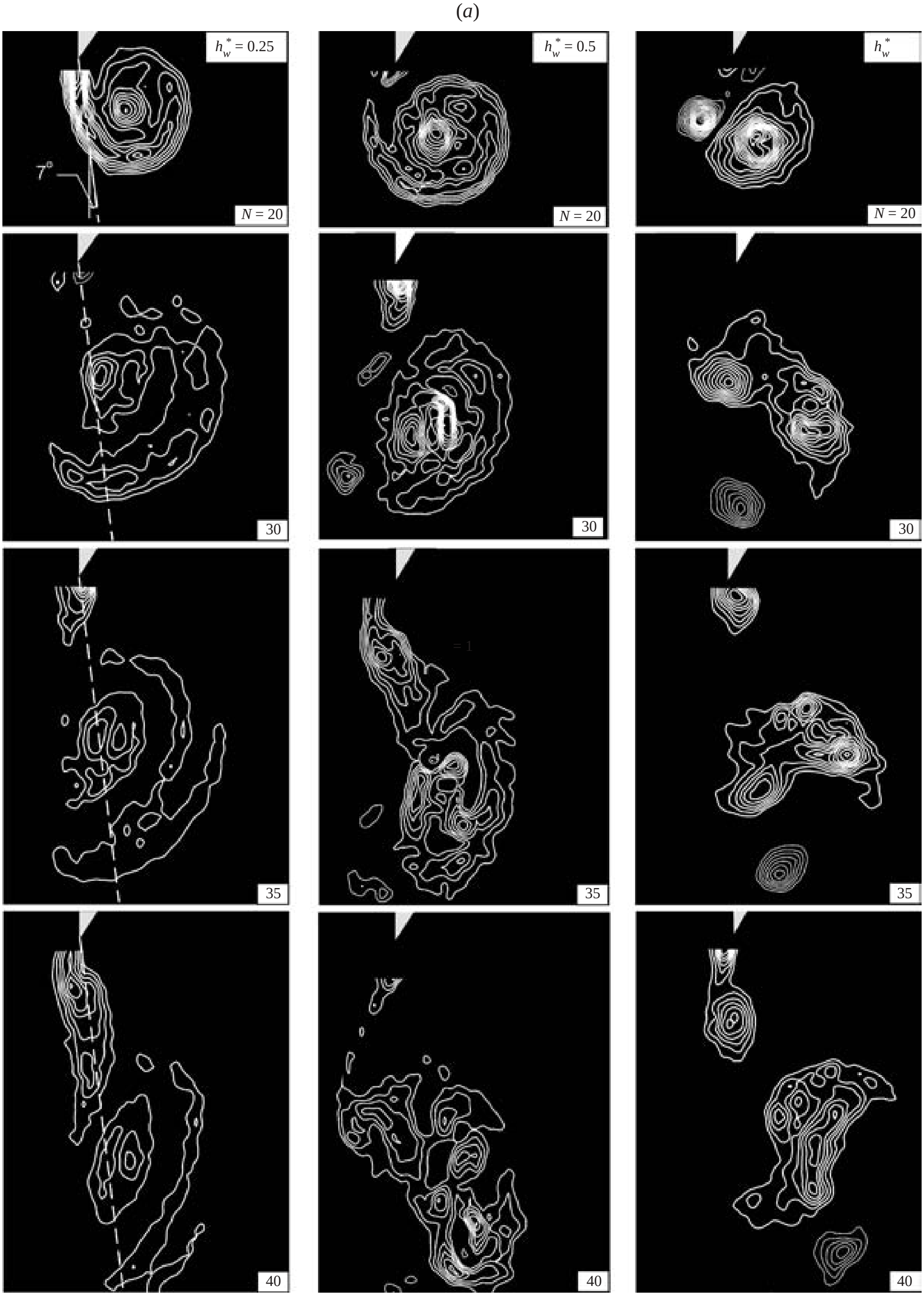

FIGURE 7. For caption see facing page.

The variation of the dimensionless circulation $\Gamma^* = \Gamma/U_pW$ is shown as a function of dimensionless time t^*, for the three values of water depth h_w^*, in figure 9(*a*). The value of Γ^* at each instant of the cinema sequence was determined by an integral of the spatially dependent vorticity $\omega(x, y, t_0)$ over the domain bounded by the lowest-level vorticity contour, which had a value $2\,\mathrm{s}^{-1}$. Only the vorticity associated

(*b*)

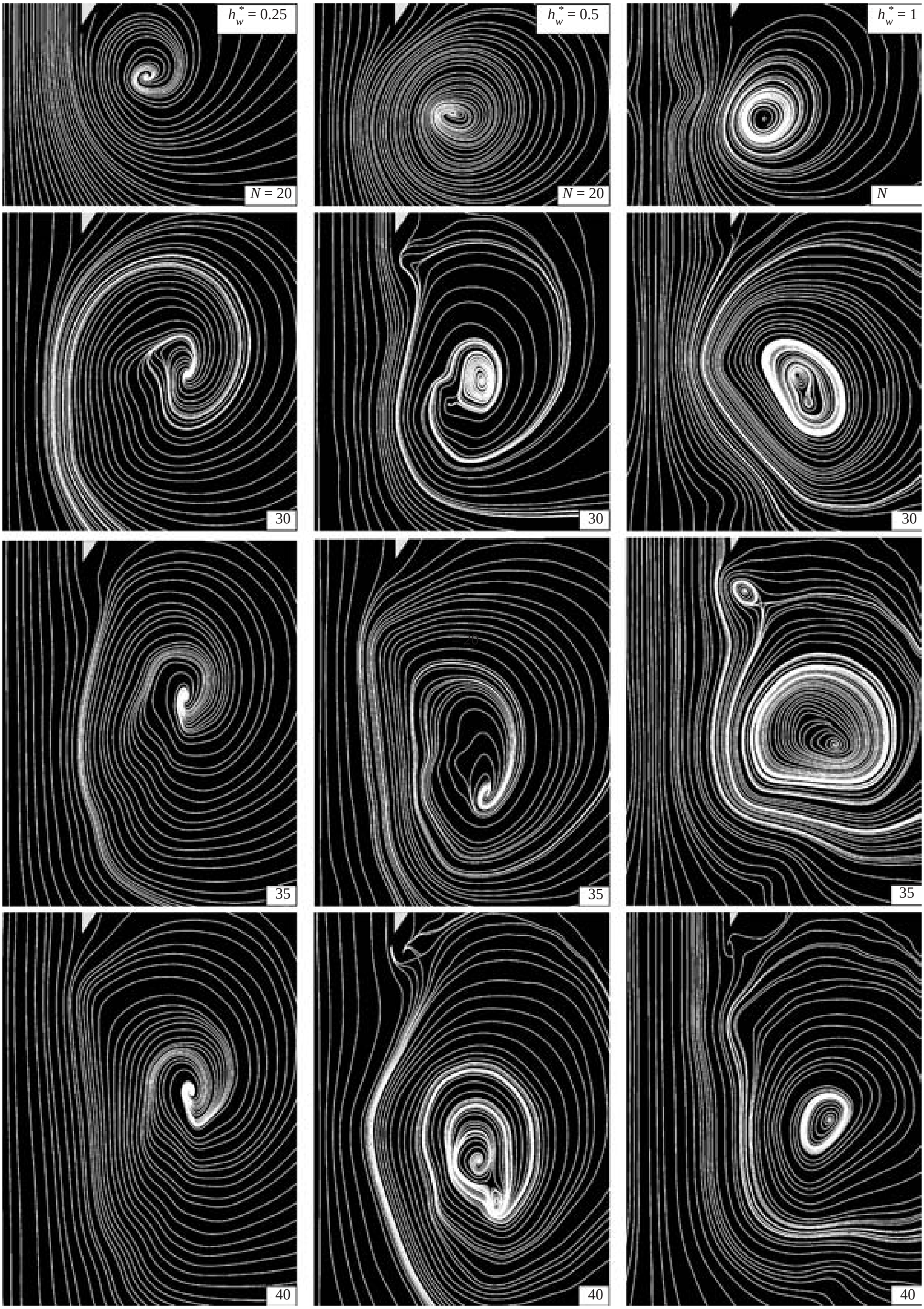

FIGURE 7. (*a*) Effect of water depth h_w^* on the development of patterns of vorticity in the plan view. In all cases, the plane of the laser sheet is located halfway between the free surface and the surface of the water table. Minimum and incremental values of vorticity are respectively $\omega_{min} = \pm 4$ and $\Delta\omega = 2\ \mathrm{s}^{-1}$. (*b*) Patterns of instantaneous streamlines corresponding to (*a*).

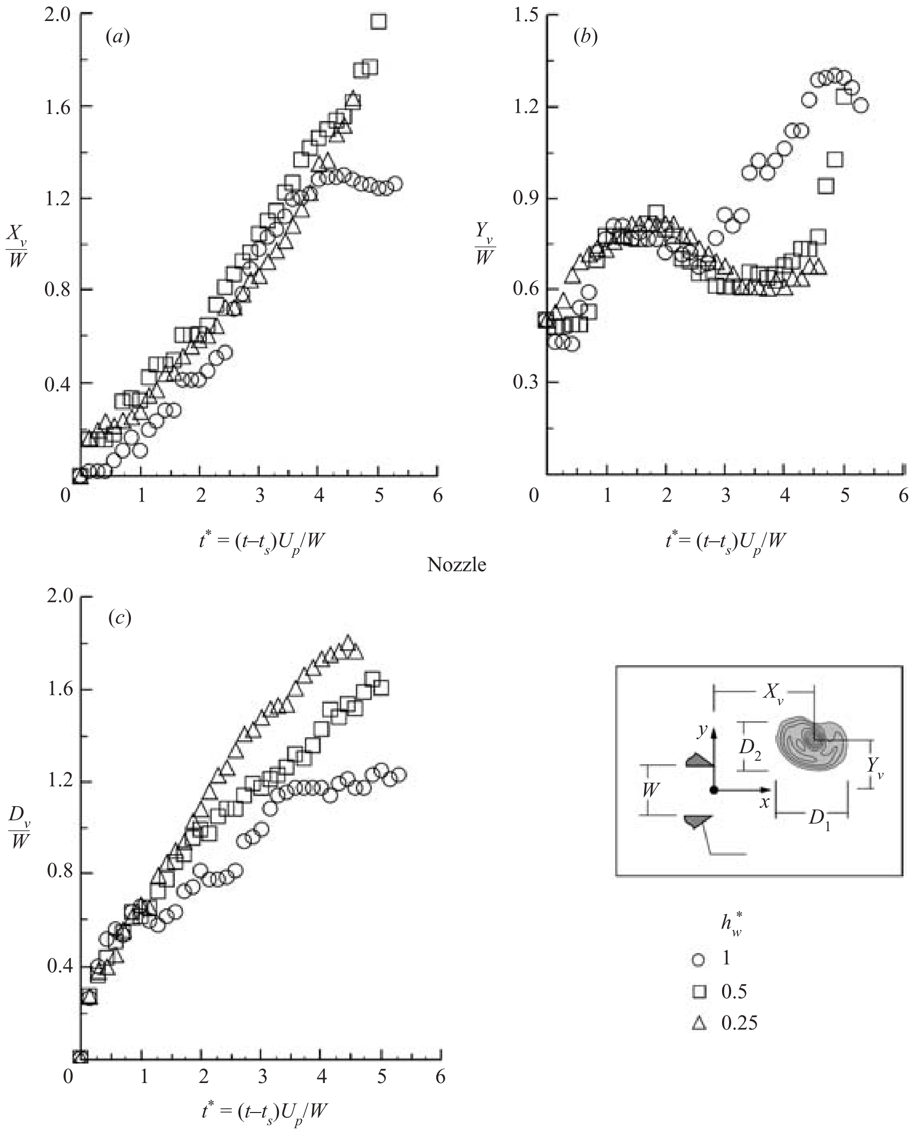

FIGURE 8. Plots of vortex position X_v, Y_v and characteristic diameter D_v as a function of water depth $h_w^* = h_w/W$.

with the major (primary) vortex formed during the first cycle was employed for calculation of Γ^*. The increase of Γ^* is approximately linear for the two shallowest water depths $h_w^* = 0.25$ and 0.5 up to a dimensionless time of the order $t^* = 0.4$. For larger values of t^*, the variation of Γ^* tends toward a flat, plateau-like distribution, then decreases. This general linear–plateau form of the dimensionless circulation Γ^* is similar to that obtained for the development of a two-dimensional (axisymmetric) vortex ring from a circular cross-section nozzle, as described by Didden (1979).

The vertical ordinate shown on the right-hand side of figure 9(*a*) corresponds to Γ/ν, which can be considered a form of Reynolds number defined in terms of a characteristic azimuthal velocity V_θ and the diameter D_v of the vortex.

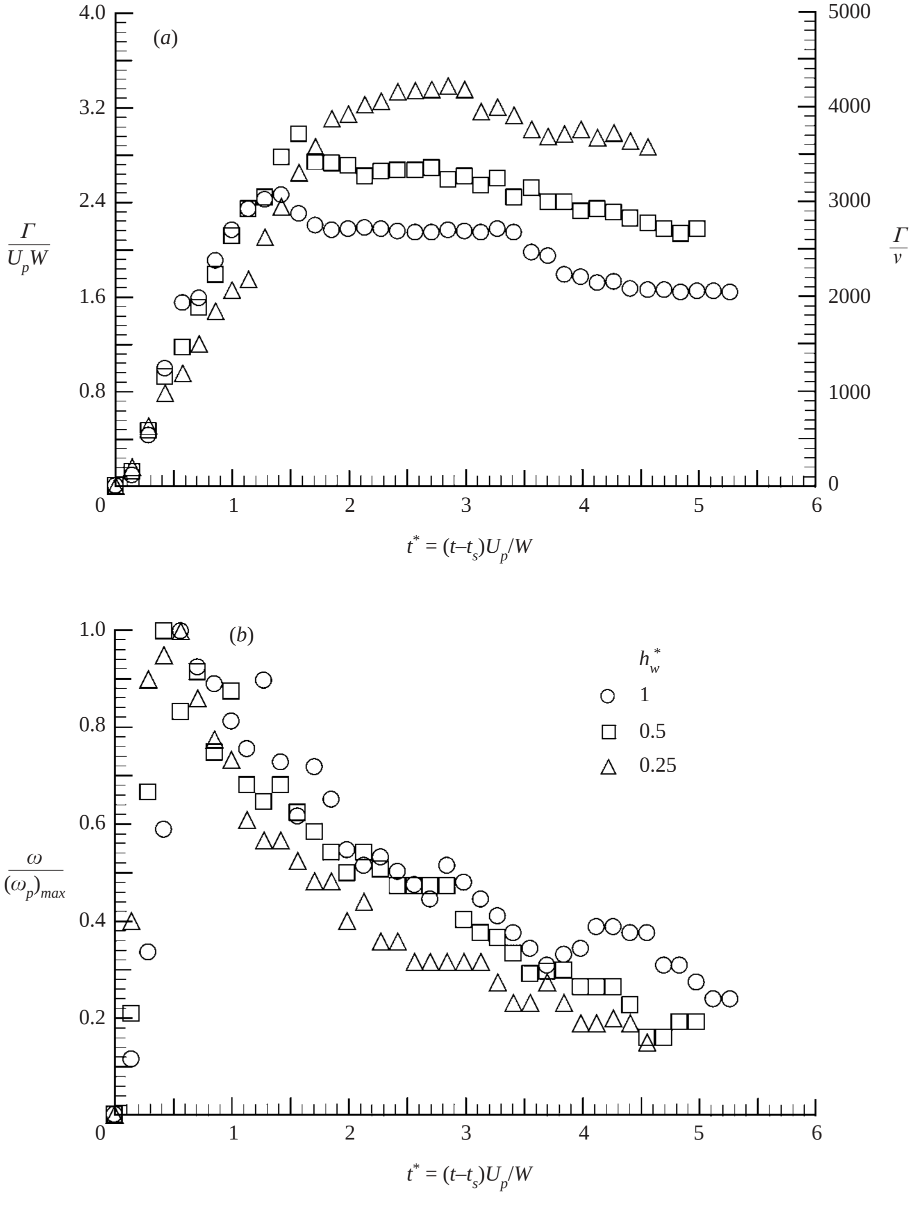

FIGURE 9. (*a*) Dimensionless circulation $\Gamma/U_P W$, Γ/ν and (*b*) normalized peak vorticity $\omega_p/(\omega_p)_{max}$ within the vortex as a function of dimensionless time t^*.

Figure 9(*b*) shows the variation of the peak vorticity ω_p within the distribution of vorticity at each instant, normalized by the maximum value $(\omega_p)_{max}$; these values correspond to the vortex formed during the first cycle of the jet velocity variation at the nozzle exit. The maximum value of peak vorticity $(\omega_p)_{max}$ was 58.4, 48 and 40 s^{-1} respectively for $h_w^* = 1$, 0.5 and 0.25. Due to strong three-dimensional effects, to be addressed below, this plot shows significant scatter. Nevertheless, it is clear that the dimensionless peak vorticity decays rapidly with dimensionless time t^*.

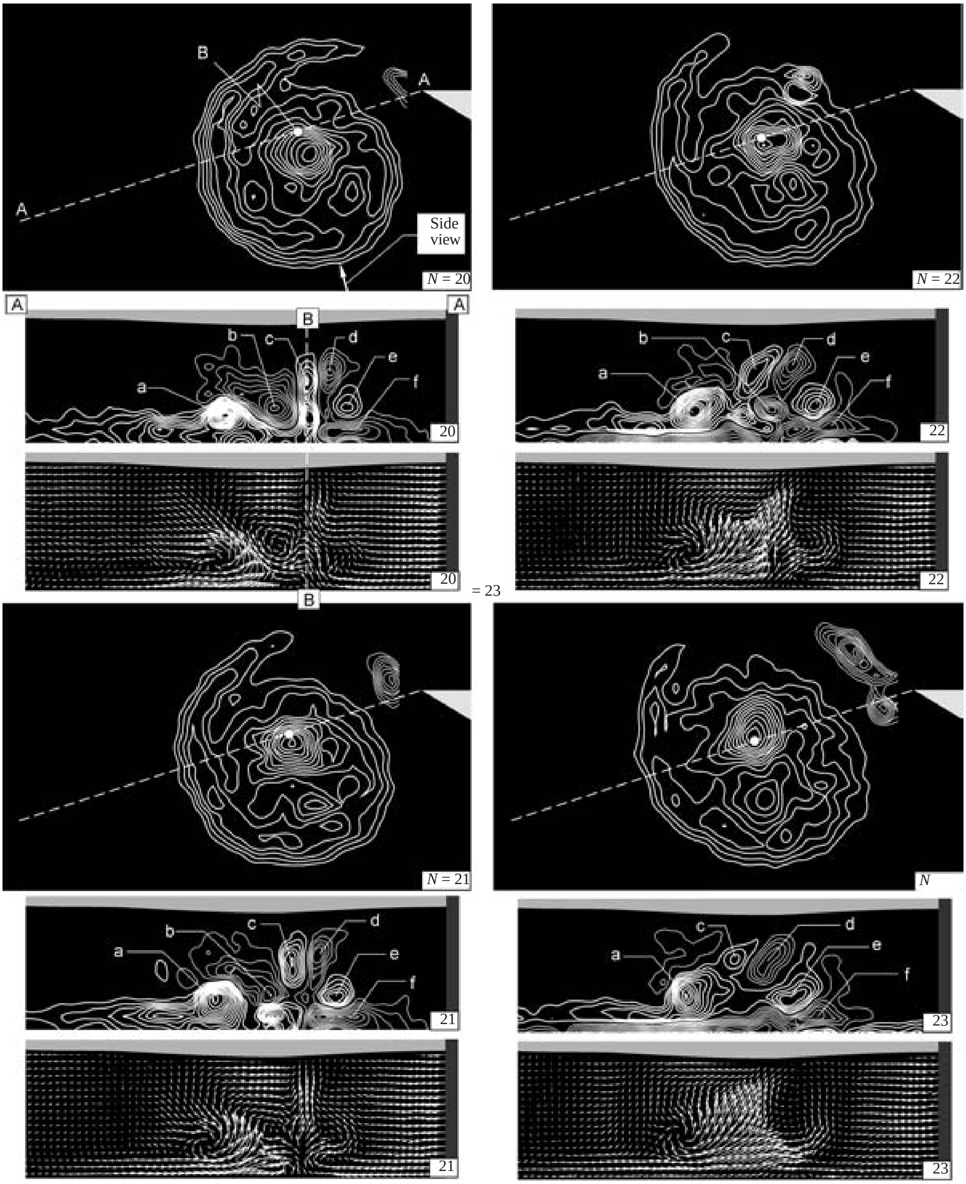

FIGURE 10. Correlated plan and side views of vortex development. Dashed line A–A indicated in the plan view represents the location of the vertical laser sheet that allows a side view. The laser sheet is at angle $\beta = 18°$ shown in figures 1 and 6. Point B represents the streamwise location of the centre of the vortex projected on the vertical laser sheet A–A. This point B in the plan view appears as a vertical line B–B in the side view. N represents the frame number of the cinema sequence. For the plan view, the minimum and incremental values of vorticity are $\omega_{min} = \pm 4\ \mathrm{s}^{-1}$ and $\Delta\omega = 2\ \mathrm{s}^{-1}$ respectively. Water depth is $h_w^* = h_w/W = 0.5$. Laser sheet for plan view is at $h_L^* = h_L/W = 0.25$ above the bottom surface. For the side view, the minimum ω_{min} and incremental $\Delta\omega$ values of vorticity are both $3\,\mathrm{s}^{-1}$.

6. Three-dimensionality of vortex development

Figure 10 directly compares plan and side views of the vortex development. The dashed white line in the plan view indicates the location of the vertical laser sheet, which is defined as A–A. The direction of the side view is indicated by the white arrow, and the streamwise location of the centre of the vortex is indicated as point B in the plan view. Point B represents the projection of the vorticity extremum on line A–A. In the side view, point B is represented as a dashed white line B–B; it serves as a reference for interpreting the patterns of vorticity and velocity. In images $N = 20$ to 22, and especially in image $N = 21$, the pattern of velocity vectors generally indicates an upward-directed flow through the centre of the vortex. This upward flow is generally consistent with the dye visualization of wake vortices from an airfoil by Koochesfahani (1989); their patterns show ejection of marker fluid away from the wall, through the centre, i.e. along the core, of the vortex.

A key feature of the vorticity patterns shown in the side views of figure 10 is the ordered arrangement of concentrations of azimuthal vorticity of alternating sign over the trailing half of the vortex, represented by d, e and f. They are located to the right of the vertical line B–B in image $N = 20$. Thick and thin white lines correspond respectively to positive (counterclockwise) and negative (clockwise) vorticity concentrations. These concentrations appear to be conceptually similar to the concentrations of azimuthal vorticity of alternating sign over the trailing half of a columnar vortex that is cut by a plate having a leading-edge orthogonal to the vortex axis, as calculated by Marshall & Krishnamoorthy (1997). A distinctive feature of the vorticity pattern of Marshall & Krishnamoorthy (1997) is that the outermost (uppermost in figure 10) concentration of azimuthal vorticity has a substantially larger value of circulation than the other concentrations. For the present configuration, all three concentrations d, e and f shown at $N = 20$ in figure 10 have commensurate values. Apparently, the highly transient nature of the vortex cutting process in the simulation of Marshall & Krishnamoorthy (1997) gives rise to an initial ring vortex, with a relatively high value of circulation based on the azimuthal component of vorticity. For the present configuration, the evolution of the three-dimensional vortex along the continuous surface is more gradual, and the succession of vortex rings suggested by the azimuthal concentrations d, e and f tend to have equal strengths.

Viewing the entire pattern of vorticity concentrations at $N = 21$, it is evident that a total of six distinct concentrations, designated as a to f, can be identified. The highest concentration of vorticity corresponds to a, which is associated with a well-defined swirl pattern of velocity vectors. This vorticity concentration a has a counterpart of opposite sign on the other side of the vertical reference line B–B; it is designated as vorticity concentration f. Likewise, concentration b has a counterpart e and concentration c extends to the same elevation d. Patterns of vorticity over the leading half of the vortex, as well as the region of the boundary layer ahead of the leading edge of the vortex, are not shown in the numerical simulations of Marshall & Krishnamoorthy (1997). Their qualitative dye visualization does show, however, a concentration of marker well ahead of the vortex, which most likely corresponds to the leading concentration a of azimuthal vorticity shown in figure 10.

The velocity image at $N = 21$ in figure 10 shows, first, a region of updraught in the pattern of velocity vectors in the central portion of the vortex. Vorticity concentration a continues to produce the most clearly defined swirl pattern of velocity vectors. In fact, the scale of the vorticity concentration a has increased somewhat relative to that in image $N = 20$, yet the concentrations of vorticity a to f are still well-defined. At a still later instant, corresponding to $N = 22$, shown in the upper right of figure 10, the identifiable vorticity concentrations continue to persist. Furthermore, a layer of negative (thin line) vorticity is now evident beneath concentration a, and extends a substantial distance to the left of concentration a. The persistence of this negative

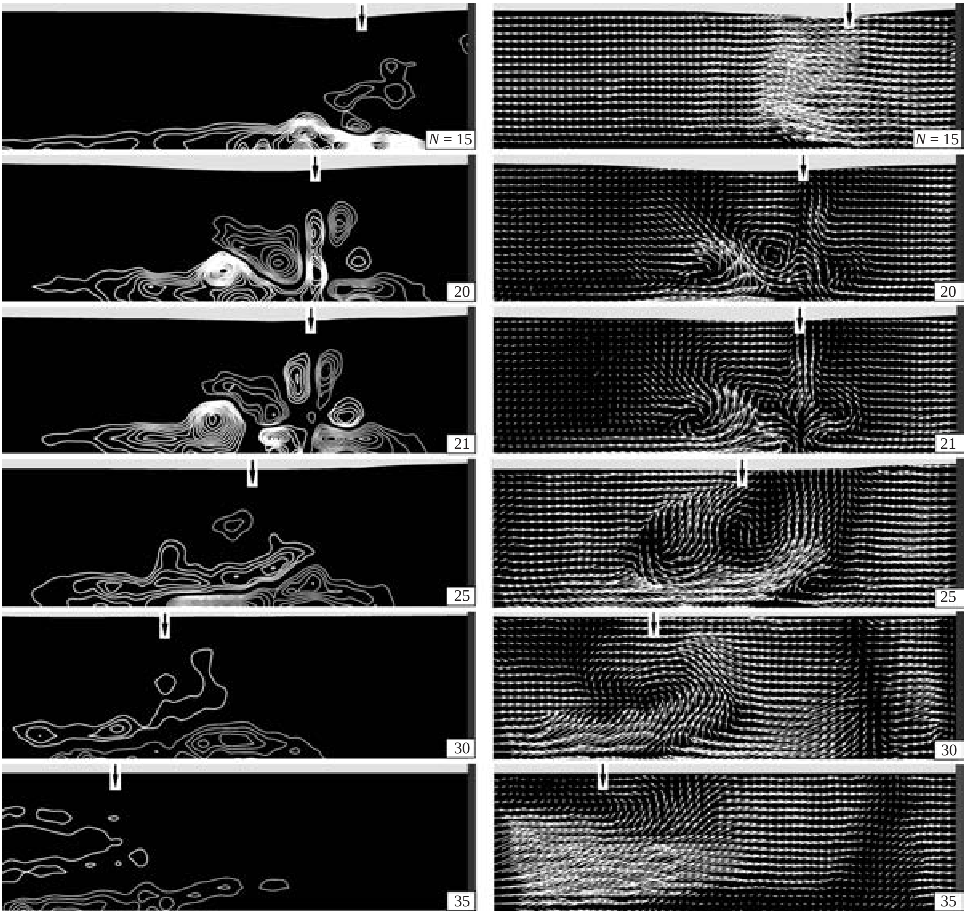

Figure 11. Comparison of the evolution with time of patterns of vorticity and velocity corresponding to the vertical cut A–A indicated in figure 10. The vertical black arrow at the free surface indicates the streamwise location of the centre of the vortex projected on A–A in figure 10. Water depth is $h_w^* = h_w/W = 0.5$. The laser sheet is at angle $\beta = 18°$, as shown in figures 1 and 6. Minimum and incremental values of vorticity are $\omega_{min} = \pm 6\,\mathrm{s}^{-1}$ and $\Delta\omega = 3\ \mathrm{s}^{-1}$.

layer immediately adjacent to the surface is also clearly evident in image $N = 23$. At this instant, nearly all of the vorticity concentrations originally observed in image $N = 20$ are still identifiable. The exception is concentration b.

Figure 11 shows the development of the patterns of vorticity and velocity extending over a long time span. All of these side view images were acquired on the plane of the laser sheet oriented at $\beta = 18°$, as defined in both figure 1 and in the plan view images of figure 6. In these and subsequent sets of images, the black vertical arrow at the free surface indicates the projection of the centre of the primary (plan view) vortex (see figure 10) on the plane of the laser sheet, as defined by the vertical line B–B in the top left set of images of figure 10. Image $N = 15$ shows the initial stage of development of vorticity concentration a, which is associated with a localized departure of the flow away from the surface; this departure is evident in the corresponding pattern of velocity vectors. At subsequent times, corresponding to $N = 20$ and 21, the development of the vorticity and velocity patterns is as described in figure 10. For the images at $N = 25$ and 30, the centre of the vortex has moved out of the plane of

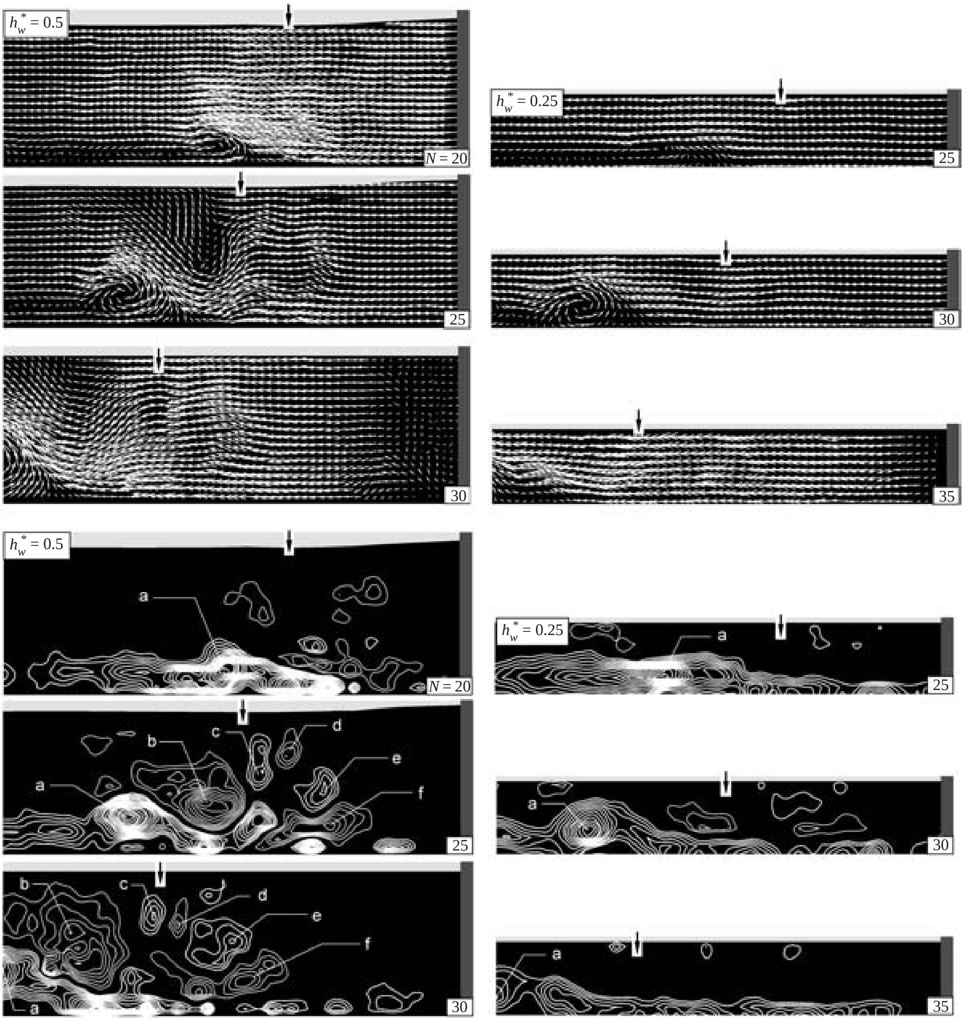

FIGURE 12. Influence of water depth on development of patterns of velocity and vorticity on the vertical plane A–A similar to that defined in figure 10. The vertical black arrow at the free surface designates the location of the centre of the vortex along the dashed line defined at $\beta = 7°$ in figure 1 and shown as $\beta = 7°$ in figure 6. Minimum and incremental values of vorticity are respectively $\omega_{min} = \pm 6\ \text{s}^{-1}$ and $\Delta\omega = 3\ \text{s}^{-1}$. Left-hand column of images corresponds to water of depth $h_w^* = h_w/W = 0.5$ and right-hand column to $h_w^* = h_w/W = 0.25$.

the laser sheet (compare plan views of figure 6). These images show that elongated regions of positive and negative vorticity adjacent to the wall are associated with inflow towards the central region of the vortex. For the remaining image, $N = 35$, only low-level regions of vorticity are evident. At $N = 35$, the corresponding plan view shown in figure 6 is relatively irregular. Nevertheless, they generally indicate that the central region of the vorticity has moved well away from the plane of the laser sheet defined at $\beta = 18°$.

Further insight into the evolution of the vortex structure is provided by the side views of figure 12, which correspond to two values of water depth, $h_w^* = 0.5$ (left-hand column) and $h_w^* = 0.25$ (right-hand column). These two sets of images both show the appearance of a pronounced swirl pattern of velocity vectors and the corresponding

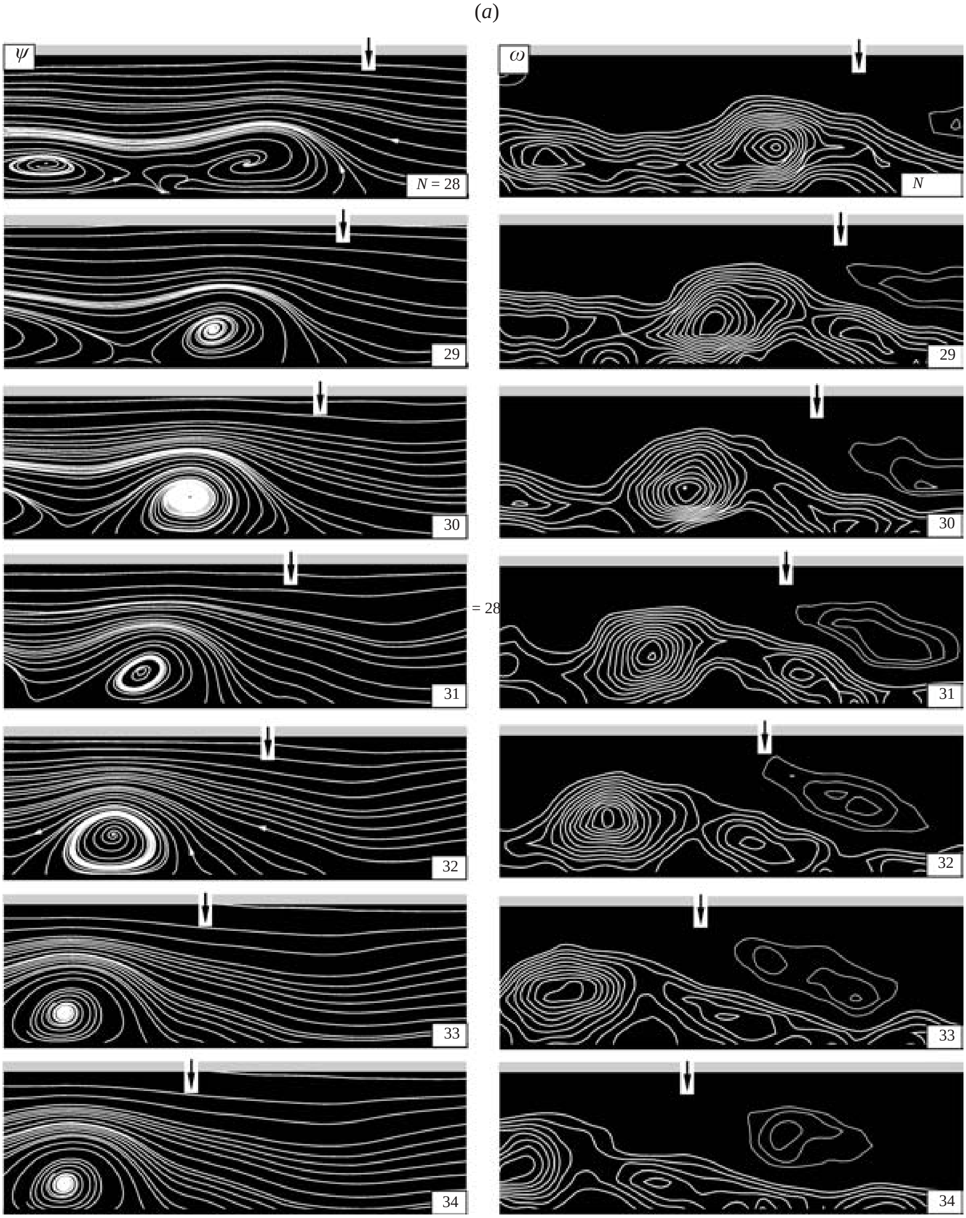

FIGURE 13. For caption see facing page.

vorticity concentration a in image $N = 25$ at $h_w^* = 0.5$ and $N = 30$ for $h_w^* = 0.25$. That is, in each of these images, the vorticity concentration a and corresponding pattern of velocity vectors occur at approximately the same spatial position from the nozzle exit. Concentration a occurs at $N = 25$ for the deeper water level, and at $N = 30$ for the relatively shallow water, thereby indicating that the development of the three-dimensional structure in the shallower water is retarded relative to that occurring in deeper water.

Consider, first, the patterns of velocity vectors shown at the top of figure 12. In the first row of images, a region of very low velocity appears adjacent to the wall. It is

(*b*)

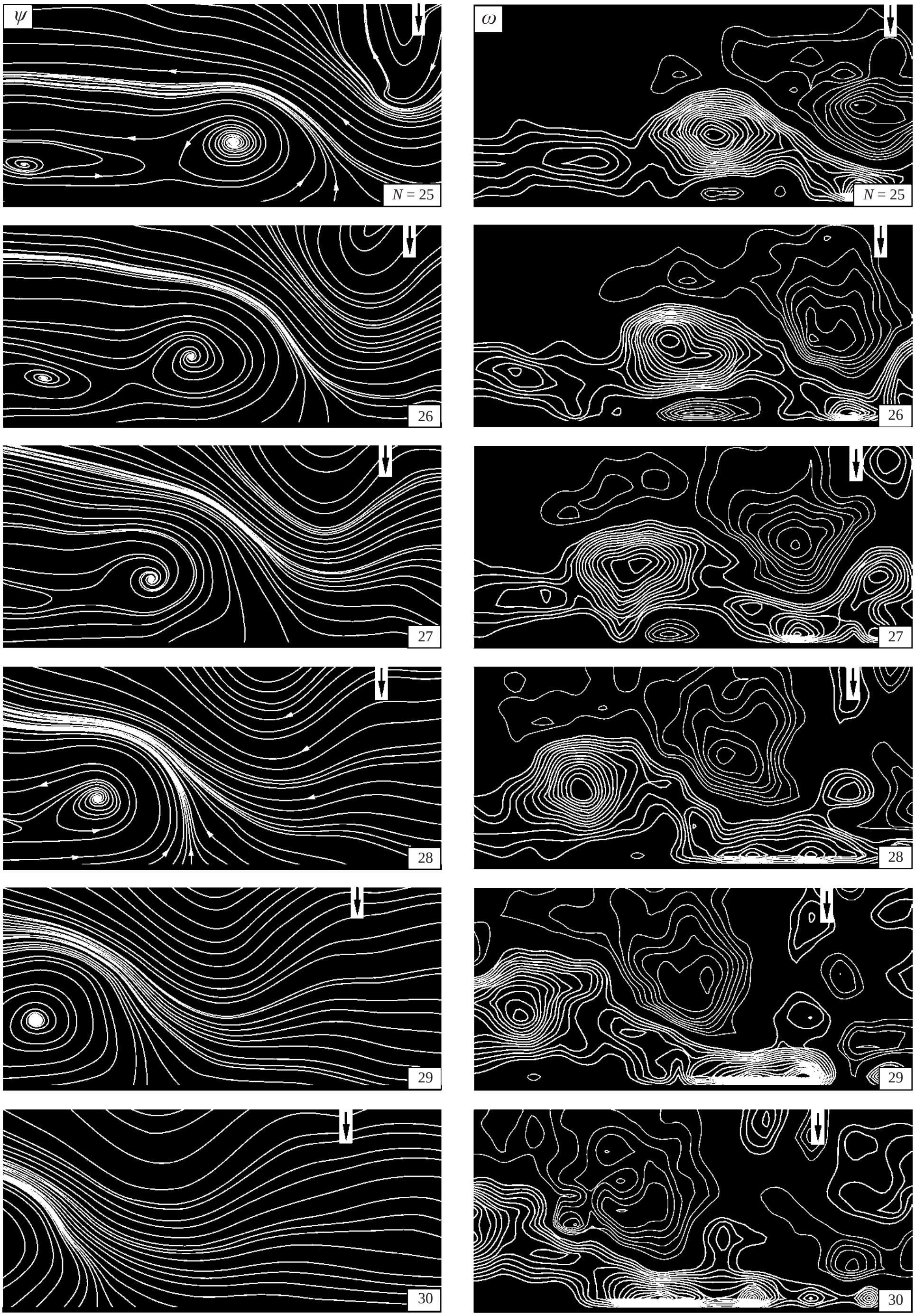

FIGURE 13. Development with time of patterns of streamline topology (left-hand column) and contours of constant vorticity (right-hand column) along a plane corresponding to the vertical cut through the dashed line indicated by $\beta = 7^\circ$ in figure 1 and figure 6. The vertical black arrow at the free-surface corresponds to the streamwise location of the centre of the vortex on the laser sheet. Depth of water is (*a*) $h_w^* = h_w/W = 0.25$ and (*b*) 0.5. Minimum and incremental values of vorticity are respectively $\omega_{min} = \pm 6\ \mathrm{s}^{-1}$ and $\Delta\omega = 3\ \mathrm{s}^{-1}$.

associated with a layer of reverse flow adjacent to the surface, which is particularly evident in the image $N = 25$ for the shallowest water, $h_w^* = 0.25$. The corresponding pattern of vorticity exhibits a relatively thick layer of positive (thick white line) vorticity extending over the entire left half of the image. A similarly thick layer of positive vorticitiy occurs at $N = 20$ for $h_w^* = 0.5$. At a later instant, corresponding to $N = 25$ for $h_w^* = 0.5$ and $N = 30$ for $h_w^* = 0.25$, the swirl pattern of velocity vectors associated with vorticity concentration *a* is well-developed. In addition, the distortion of the velocity field extends across the entire depth of the deeper water $h_w^* = 0.5$, $N = 25$. Correspondingly, in the vorticity image at $N = 25$ ($h_w^* = 0.5$), not only concentration *a*, but also a number of other distinguishable concentrations are evident, especially concentration *b*, which has a particularly large scale and circulation. (This arrangement of vorticity concentrations is very similar to that observed in figure 10 at instant $N = 20$ for a different angle of inclination of the laser sheet.) In contrast, only a single, pronounced concentration of vorticity is suggested in the velocity field $N = 30$ ($h_w^* = 0.25$) for the case of shallower water. The corresponding plot of vorticity at $N = 30$ ($h_w^* = 0.25$) shows that this is indeed the case.

At a still later instant, corresponding to $N = 30$ for the deeper water ($h_w^* = 0.5$), the velocity swirl pattern and the concentration of vorticity *a* have nearly moved out of the field of view, leaving a distortion of the velocity field that is primarily due to vorticity concentration *b*, along with secondary distortions associated with the smaller-scale concentrations. In the image for the shallow water at $N = 35$ ($h_w^* = 0.25$), velocity and vorticity representations of concentration *a* have also nearly moved out of the field of view, leaving only a positive vorticity layer adjacent to the wall. Viewing the patterns of velocity and vorticity of figure 12 together, it is evident that sufficiently shallow water suppresses the development of other significant concentrations of vorticity; in deeper water, the pattern of concentrations can extend over the entire depth.

The development with time of the vorticity concentration *a* (compare figure 12), and the corresponding sectional streamline topology in relatively shallow water ($h_w^* = 0.25$) is indicated in figure 13(*a*). The vertical arrows indicate the location of the projected centre of the primary (plan view) vortex on the plane of the laser sheet, i.e. the plane of the image. As the value of N increases, the identity of vorticity concentration *a* becomes more distinct. (Compare figure 12, vorticity images $N = 25$, 30, and 35). The corresponding streamline topology shows the occurrence of a separatrix, i.e. a half-saddlepoint at the surface, for all values of N. The topology of the vortex transforms to a well-defined limit cycle, evident at $N = 32$. Then, degeneration of the limit cycle occurs at larger values of N.

On viewing together the patterns of vorticity at $h_w^* = 0.25$ in figure 12, as well as the time-resolved patterns of vorticity and velocity in figure 13(*a*), certain features appear to be analogous to patterns arising from vortex-induced separation in strictly two-dimensional flows. For the case of translation of a rectilinear vortex along a wall, it is possible to induce focused separation from the wall, as shown by Walker (1978), and in the extensive series of subsequent investigations reviewed by Doligalski, Smith & Walker (1994). A consequence of this two-dimensional separation process is the generation of a separation bubble behind the primary (parent) rectilinear vortex. This sequence of streamline patterns in figure 13(*a*) shows, in essence, the evolution of such a separation bubble and the corresponding vorticity concentration. The investigations of two-dimensional vortex–wall interaction assessed by Doligalski *et al.* (1994) also show that the separation bubble remains attached to the wall when viewed in the laboratory reference frame. For the present series, the primary (parent) vortex is shown in the left-hand column of figure 6, and its centre is designated by the vertical arrows in figure 13(*a*). The distinguishing feature, relative to the aforementioned two-dimensional vortex system, is that the primary vortex is orthogonal to the concentration of vorticity associated with the separation bubble. A further distinction is that the separation bubble is located ahead of, rather than behind, the primary vortex.

The corresponding patterns of streamline topology and vorticity for deeper water are shown in figure 13(*b*). In the region near the wall, the onset of vorticity concentration *a* (compare figure 12) is very similar to that described for the shallower water in figure 13(*a*). Concentration *a* (thick white lines) again occurs ahead of the centre of the primary (plan view) vortex. The additional formation of large-scale concentration *b* (contours of thin white lines), and the subsequent concentrations evident at larger values of N, is associated with severe distortion of the streamline topology. (Compare vorticity patterns of figure 12, $N = 25$ and 30, for vortices *a* and *b*.) In all images, a streamline intersecting the bottom surface is clearly evident, corresponding to a separatrix at that location.

7. Near-surface consequences of vortex evolution in shallow water

The quasi-two-dimensional and three-dimensional vortex development in regions above the surface, which are characterized in the foregoing, will have consequences for the spatial distributions of velocity and vorticity very near the bottom surface (bed). In order to characterize the global, instantaneous features of the near-surface region, the laser sheet was located as close to the surface as possible, corresponding to $h_L^* = h_L/W = 0.03$. Figure 14 compares the patterns of instantaneous vorticity (middle column) and velocity (right-hand column) in this near-surface region with corresponding distributions of vorticity at the mid-depth of the water (left-hand column). For images $N = 20$ and 25, it is evident that the footprint of the large-scale vortex motion in the near-surface region mimics, in a global sense, that characterized at the midplane. At larger values of $N = 30$ and 35, the overall form of the region of vorticity in the near-surface region is substantially distorted relative to that at the midplane. A remarkable consequence of the vorticity pattern in this near-surface region is the occurrence of small-scale concentrations of positive and negative vorticity, which are spatially distributed in an alternating sense across the region between the two large-scale vortices produced in the jet, as well as within the footprint of the large-scale vortex. These vorticity concentrations have a typical value of dimensionless circulation $\Gamma^* = \Gamma/\pi U_p D_v = 0.06$, in which U_p is the piston velocity and D_v is the characteristic diameter of the small-scale vorticity concentration. These values compare with $\Gamma^* = 0.8$ of the initially formed, large-scale vortex, depicted, for example, in the image $N = 20$ at the upper left of figure 14. The corresponding velocity fields show pockets of low, nearly zero, velocity along the bottom surface (bed). They are related to the occurrence of large spatial gradients along the front of the developing jet–vortex structure. It appears that the advancing front of the jet–vortex system induces a number of streamwise striations across the front, which are evident in independent dye visualization. These striations are shown in the region immediately downstream of the nozzle exit in figure 19, which will be addressed below. Since these striations are indicative of a nonlinear process, which is highly three-dimensional, the signatures of instantaneous small-scale concentrations of vorticity ω_y normal to the bottom surface (bed) are representative indicators. These small-scale concentrations of vorticity of figure 14, which, viewed as a whole, indicate a quasi-ordered pattern of three-dimensionality, may have analogies to the phenomena of nonlinear transition

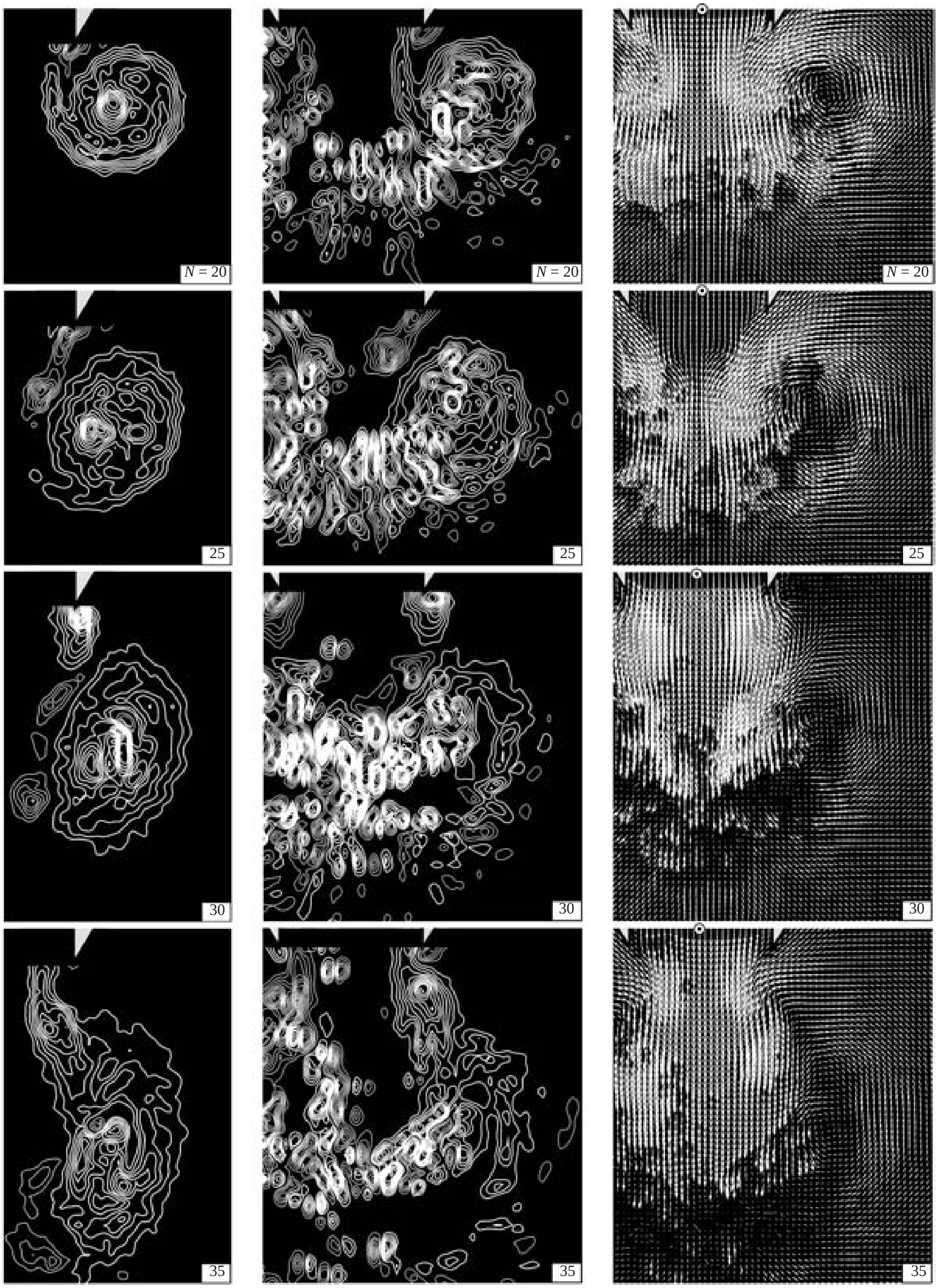

FIGURE 14. Patterns of instantaneous vorticity at mid-plane $h_L^* = h_L/W = 0.25$ between the free-surface and the bottom surface of the table (left-hand column), at a distance of $h_L^* = h_L/W = 0.03$ above the bottom surface of table (middle column) and corresponding patterns of instantaneous velocity at $h_L^* = h_L/W = 0.03$ (right-hand column). Water depth is $h_w^* = h_w/W = 0.5$. Minimum and incremental values of vorticity are both 2 s^{-1} for all images.

of a well-posed boundary layer along a flat plate. Clearly, the present situation of an abrupt change in boundary conditions at the jet nozzle exit and subsequent evolution of the near-surface layer in the presence of a vertical primary vortex is considerably more complex than the classical evolution of Tollmien–Schlichting waves in a boundary layer along a flat plate. It is well-known that the onset of the nonlinear stage of transition yields spanwise variations of velocity and longitudinal (streamwise) concentrations of vorticity. Spanwise variations of fluctuation velocity are evident from the pointwise velocity measurements of Klebanoff, Tidstrom & Sargent (1962) and several classes of Λ-type unstable vortex breakdown in a boundary layer are defined by Saric & Thomas (1984) using a smoke wire visualization technique. These patterns were classified according to whether they were in-line or staggered. The spanwise wavelength λ_z was one-half the streamwise wavelength. For the present experiment, it is difficult to define an equivalent streamwise wavelength. A further perspective involves the late stage of transition of a boundary layer along a flat plate. Turbulent bursts appear in the form of spots. Within such spots, streamwise striations are evident, as indicated by the visualization of Cantwell, Coles & Dimotakis (1978). In view of the complex initial conditions and evolution of the present small-scale three-dimensionality, it is not possible to establish a conclusive link to the foregoing idealized cases of rich transition phenomena occurring in the classical boundary layer along a flat plate.

Representations of the averaged flow structure are shown in figure 15. They were obtained from a total of 36 images, which extended from $N = 7$ to $N = 42$. The top row of images corresponds to the location of the laser sheet midway between the surface and the bottom, i.e. $h_L^* = h_L/W = 0.25$, whereas the bottom row is at $h_L^* = 0.03$; these are at the same locations of the laser sheet as employed for figure 14. Consider, first, the patterns of vorticity shown in the left-hand column. The averaged image at the midplane shows an extended region of relatively low-level vorticity having an extremum close to the nozzle exit. Close to the bottom surface, however, the pattern exhibits small-scale concentrations. In the central region of the jet flow, these small-scale highly concentrated regions of vorticity are still clearly identifiable relative to those shown in the instantaneous images of figure 14. This suggests that they are nearly stationary in time.

The patterns of averaged velocity, given in the middle column of figure 15, show a large-scale swirl and an overall pattern of velocity in the central region of the jet that is generally similar for both midplane and near-bottom locations. Finally, the patterns of streamlines shown in the right-hand column exhibit a remarkably similar form. Both have an unstable focus. The averaged topology at the surface is therefore a reliable footprint of the averaged topology above it, e.g. at the midplane.

8. Repeatability of flow patterns

Indications of the repeatability of the patterns of vorticity discussed above are given in figures 16 and 17. These images were acquired at the same value of N for different experimental runs. Plan views of the instantaneous concentrations of vorticity, acquired at the midplane, are shown in figure 16. Direct comparisons are given at instants $N = 21$, 30 and 40. The overall form of the vorticity concentrations and, more importantly, the existence and location of region(s) of highly concentrated vorticity, are evident in the early and intermediate stages of development of the vortex, i.e. $N = 21$ and 30. In the later stages, these features are still directly comparable, though the equivalence is not as precise. Side views of the flow structure, exhibited

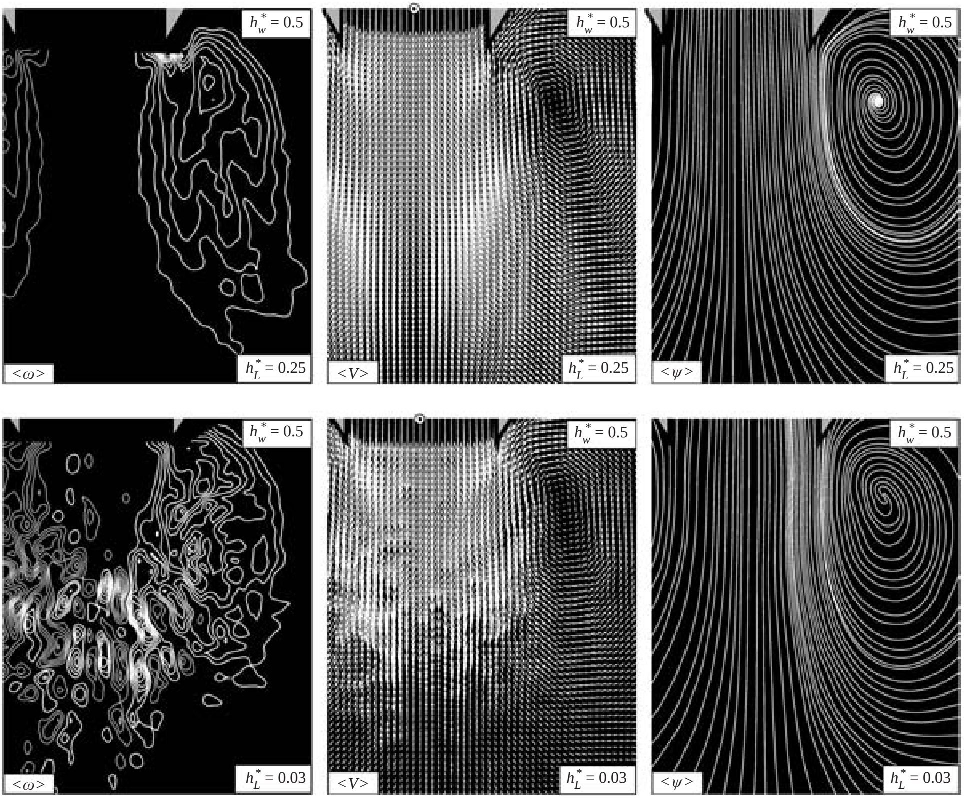

FIGURE 15. Effect of laser sheet location $h_L^* = h_L/W$ on plan views of patterns of averaged vorticity $\langle\omega\rangle$, streamline $\langle\psi\rangle$ and velocity vector fields $\langle V\rangle$. Depth of water is $h_w^* = h_w/W = 0.5$. Minimum $\langle\omega_{min}\rangle$ and incremental $\Delta\omega$ values of averaged vorticity are both 1 s^{-1}.

in figure 17, indicate that the location of concentrations of vorticity appears to be repeatable with relatively high fidelity, in both space and time.

A further comparison involves patterns of vorticity immediately above the surface of the bed, as shown in figure 18. For this comparison, as for figure 14, the laser sheet is located at $h_L^* = h_L/W = 0.03$. The right-hand image shows a larger number of small-scale vorticity concentrations immediately below the primary large-scale vortex, relative to the patterns shown in the left image. It is evident that the onset of nonlinear transition phenomena in the near-wall region is highly sensitive to extremely small variations in the vortex generation process; the conditions for generation were the same for the two images of figure 18 within the bounds of experimental uncertainty. That is, the small-scale phenomena of figure 18 clearly do not show the same degree of high fidelity of repeatability as for the images of figures 16 and 17.

9. Dye visualization

Figure 19 shows an overview of qualitative dye visualization for the three values of dimensionless water depth $h_w^* = 0.25$, 0.5 and 1.0. In all cases, the dye was placed on the surface of the water table; it extended along a line across the exit of the jet nozzle. For the shallowest water of $h_w^* = 0.25$, the first image shows the formation of 'kinks' in the dye pattern and, at successively larger times, the streamwise location of this

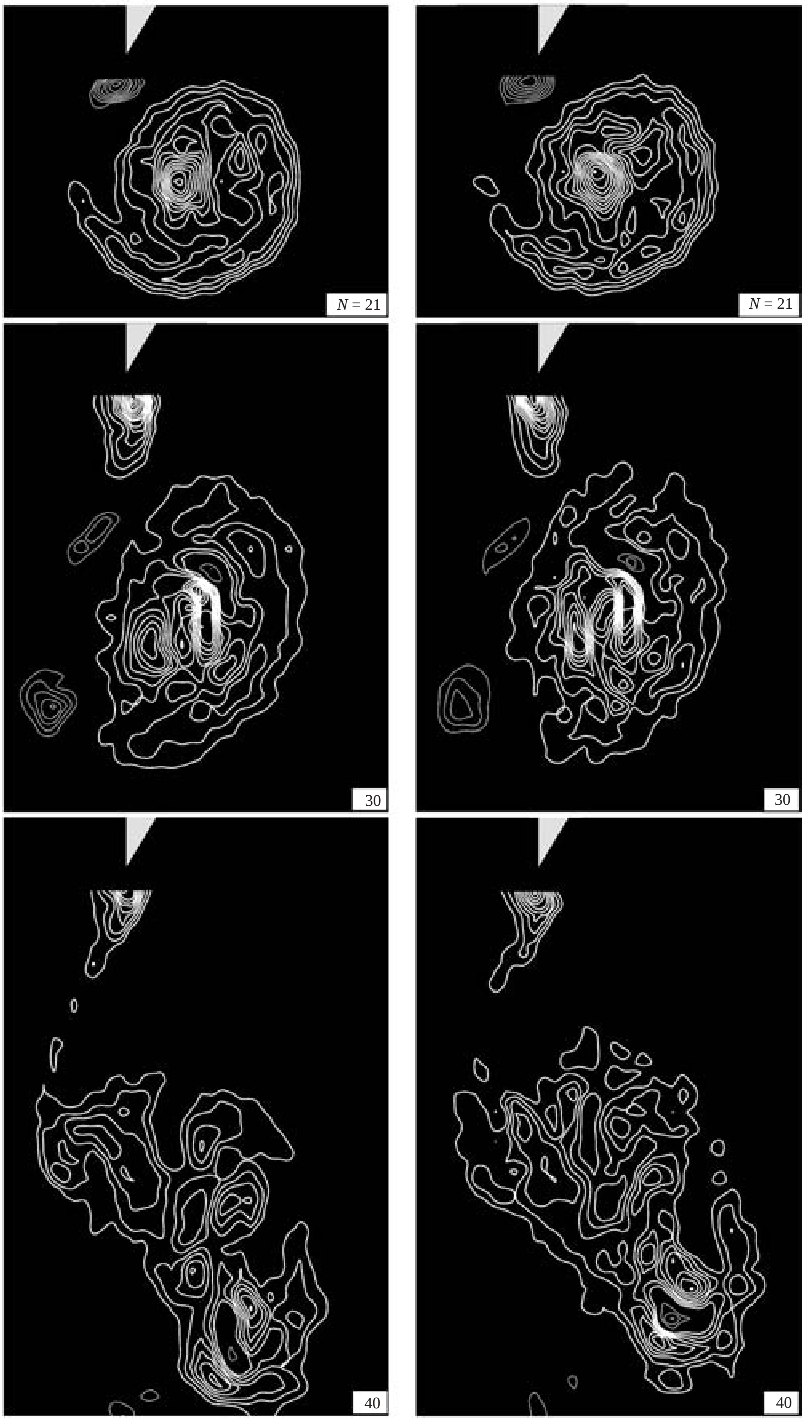

FIGURE 16. Comparisons of patterns of instantaneous vorticity obtained from two independent experimental runs. Water depth is $h_w^* = h_w/W = 0.5$ and the laser sheet is $h_L^* = h_L/W = 0.25$ above the bottom surface of the table. Minimum and incremental values of vorticity are respectively $\omega_{min} = \pm 4\ \mathrm{s}^{-1}$ and $\Delta\omega = 2\ \mathrm{s}^{-1}$.

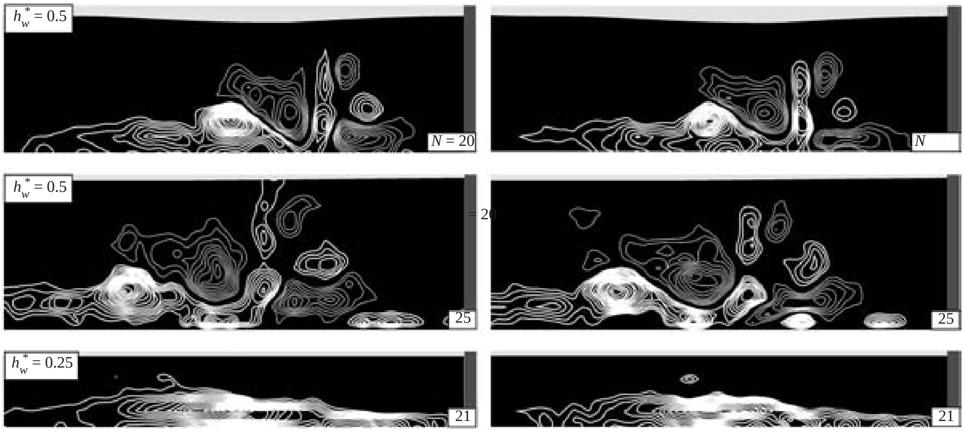

FIGURE 17. Comparison of patterns of vorticity corresponding to the side view, acquired during two different experimental runs. The top and middle row of images correspond to a water depth of $h_w^* = h_w/W = 0.5$, and an angle of inclination $\beta = 18°$ in the first row and $\beta = 7°$ in the second as defined in figure 1; minimum and incremental values of vorticity are respectively $\omega_{min} = \pm 6$ s^{-1} and $\Delta\omega = 3$ sec^{-1}. Bottom row of images corresponds to a depth $h_w^* = h_w/W = 0.25$, and $\beta = 7°$; minimum and incremental values of vorticity are respectively $\omega_{min} = \pm 9$ s^{-1} and $\Delta\omega = 3$ s^{-1}.

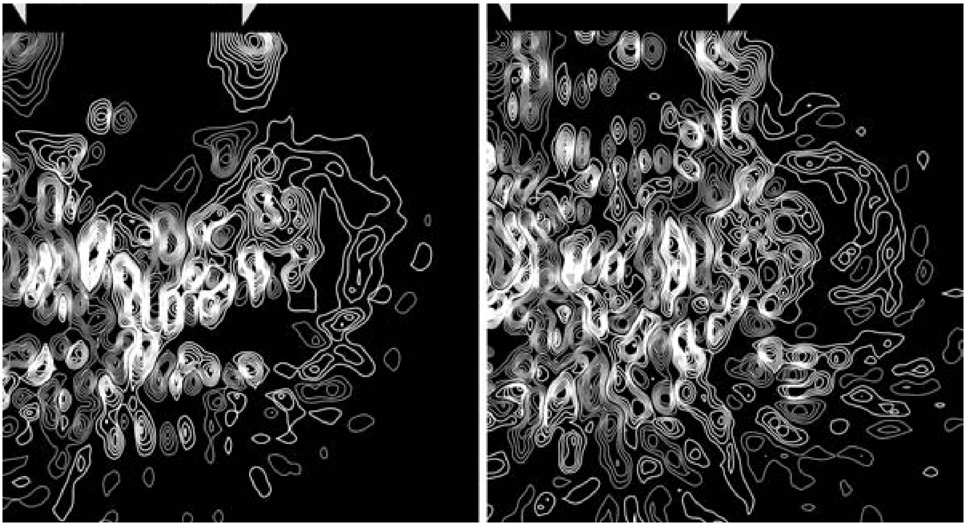

FIGURE 18. Comparisons of patterns of instantaneous vorticity obtained from two independent experimental runs at $N = 30$. Water depth is $h_w^* = h_w/W = 0.5$ and laser sheet is at $h_L^* = h_L/W = 0.03$ above the bottom surface of the table. Minimum and incremental values of vorticity are both $\omega_{min} = \pm 2$ s^{-1} for both images.

localized distortion of the dye moves downstream. In addition, the leading front of the dye lines progresses downstream as well. In the middle row of images, $h_w^* = 0.5$, the initial distortion of the dye pattern appears to take the form of concentrated swirls, which take on larger-scale and more complex forms at later values of time. Likewise, in the right-hand column of images, at $h_w^* = 1.0$, the region of distorted dye becomes remarkably concentrated in the first image and exhibits intense activity

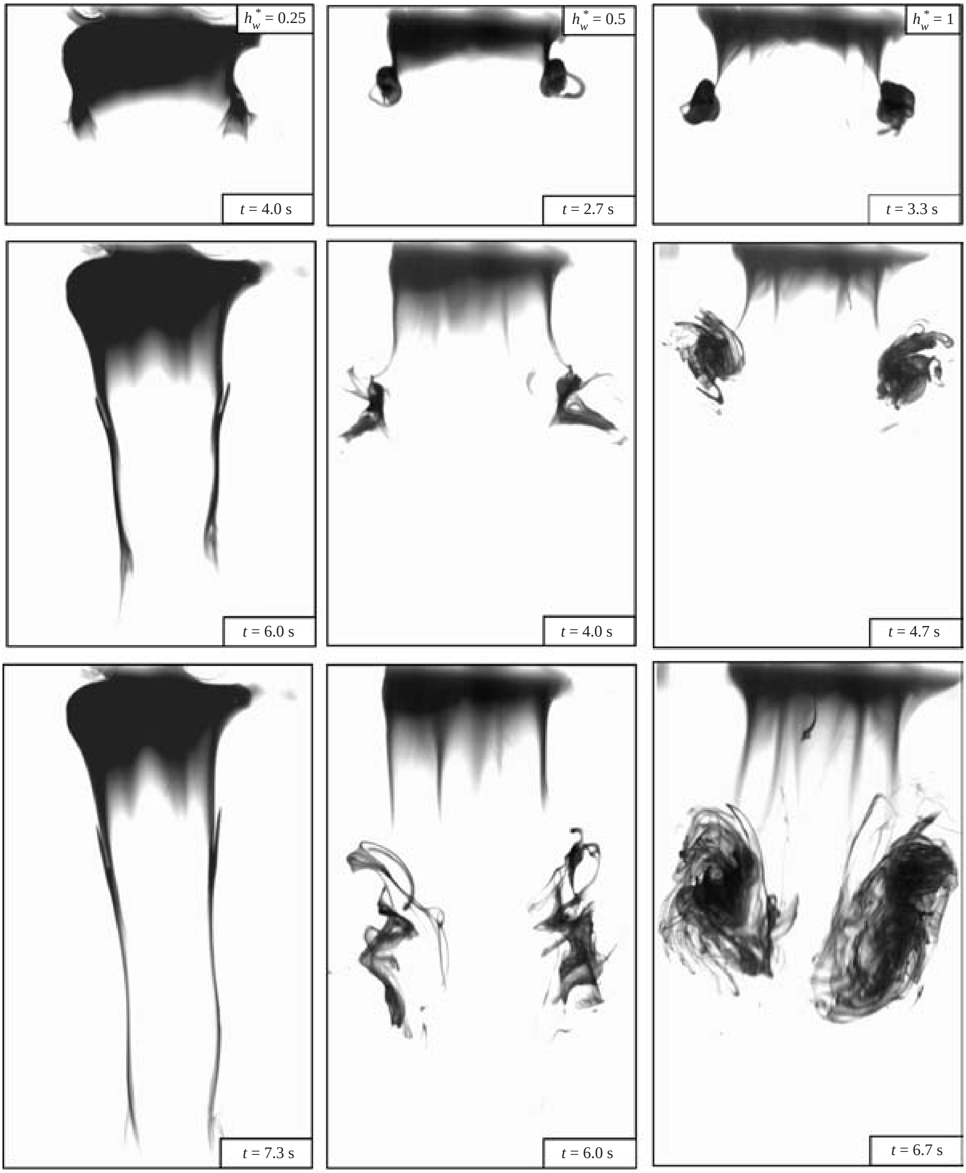

FIGURE 19. Dye visualization showing the effect of h_w^* on the development of the flow structure. Dye was placed on the bottom surface of the water table at the nozzle exit, prior to the start of the piston motion.

in subsequent images. Taking an overview of the images corresponding to all three values of water depth h_w^*, it is possible to make the following observations. For the shallowest water $h_w^* = 0.25$, the flow distortion is confined to a region relatively close to the bottom surface (bed), whereas for the larger values of h_w^*, the dye pattern extends over a region of larger spatial extent above the bottom surface. In fact, the images of velocity and vorticity indicate that this is the case. That is, sufficiently shallow water suppresses the development of vortical activity at larger distances from the bottom surface.

10. Concluding remarks

Controlled generation of a vortex system in an impulsively started jet flow yields highly repeatable patterns of quasi-two-dimensional and three-dimensional flow structure, which are characterized using a technique of digital particle image velocimetry. Emphasis is on the case of vortices in shallow water for which the characteristic diameter of the vortex is larger than the water depth.

The distributions of vorticity of the primary vortex, when observed in the plan view at the mid-depth of the water layer, rapidly evolve to different forms, which are dictated by water depth. All are characterized, however, by the occurrence of a small-scale region of highly concentrated vorticity within the larger cluster of distributed vorticity. The magnitude(s) of the peak vorticity in the cluster of vorticity decays rapidly for all values of water depth. Moreover, when the value of dimensionless water depth is sufficiently small, the plots of vortex position, diameter and circulation show remarkably similar variations with dimensionless time. These observations are intimately related to the nature of the three-dimensionality. Highly coherent and repeatable patterns of vorticity concentrations, which have an orientation orthogonal to that of the primary (plan view) vortex, are generated in a repeatable fashion for the extreme values of water depth considered herein.

For the case of the shallowest water, an out-of-plane vorticity concentration, i.e. a concentration orthogonal to the primary large-scale vortex, is formed at the forward edge of the primary vortex. Its streamline pattern, taken together with its vorticity pattern, indicates a separation bubble that translates along the wall, in analogy to the classical bubble induced by a two-dimensional vortex along a surface (wall). Sufficiently shallow water inhibits the formation of additional concentrations of vorticity.

On the other hand, when the water depth becomes sufficiently large, a highly ordered array of vorticity concentrations, orthogonal to the primary (parent) vortex, is formed in the region extending from the leading edge of the primary (plan view) vortex through its central region. This array includes an orthogonal vortex formed near the bottom surface and located at the leading edge of the primary large-scale vortex, in the same manner as in shallow water. Again, this pattern of vorticity, in conjunction with the streamline pattern, defines a separation bubble, which occurs along the bottom surface.

These quasi-two-dimensional and three-dimensional patterns of vorticity formed above the bottom surface occur in conjunction with large spatial gradients of velocity and vorticity in a plane close to the bottom surface (bed). Small-scale alternating positive and negative concentrations of vorticity are evident in the near-surface layer across the entire extent of the jet–vortex system. Their spanwise wavelength is an order of magnitude smaller than the scale of the primary vortex.

The authors are grateful to the National Science Foundation for support of this research under Grant No. CTS-9803734. In addition, supplemental financial support was provided by the Office of Naval Research on Grants N00014-94-1-0815 and N00014-99-0581.

REFERENCES

Adrian, R. J. 1991 Particle-imaging techniques for experimental fluid mechanics. *Annu. Rev. Fluid Mech.* **23**, 261–304.

Akilli, H. & Rockwell, D. 2002 Vortex formation from a cylinder in shallow water: flow structure and topology. *Phys. Fluids* **14**, 2957–2967.

Alavian, V. & Chu, V. H. 1985 Turbulent exchange flow in a shallow compound channel. *Proc. 21st Congress of International Association of Hydraulic Research*, Vol. 3, pp. 446–451.

Balachandar, R., Chu, V. H. & Zhang, J. 1997 Experimental study of turbulent concentration flow field in the wake of a bluff body. *Trans. ASME: J. Fluids Engng* **199** 263–270.

Balachandar, R., Ramachandran, S. & Tachie, M. F. 2000 Characteristics of shallow turbulent near wakes at low Reynolds numbers. *Trans. ASME: J. Fluids Engng* **122**, 302–308.

Balachandar, R., Tachie, M. F. & Chu, V. H. 1999 Concentration measurement in intermediate shallow wakes. *Trans. ASME: J. Fluids Engng* **121**, 34–43.

Best, J. L. & Roy, A. G. 1991 Mixing-layer distortion at the confluence of channels of different depth. *Nature* **350**, 411–413.

Biron, P., Roy, A. G. & Best, J. L. 1996 Turbulent flow structure at concordant and discordant open-channel confluences. *Exps. Fluids* **21**, 437–446.

Cantwell, B., Coles, D. & Dimotakis, P. 1978 Structure and entrainment in the plane of symmetry of a turbulent spot. *J. Fluid Mech.* **87**, 641–672.

Chen, D. & Jirka, G. H. 1986 Linear stability analysis of turbulent mixing layers and jets in shallow water layers. *J. Hydraul. Res.* **36**, 815–830.

Chen, D. & Jirka, G. H. 1993 Flow visualization and absolute instability analyses for plane wakes bounded in a shallow water layer. In *Advances in Hydro-Science and Engineering* (ed. S. Y. Wang), Vol. 1, p. 1124. Center for Computational Hydroscience and Engineering, the University of Mississippi.

Chen, D. & Jirka, G. H. 1995 Experimental study of plane turbulent wakes in a shallow water layer. *Fluid Dyn. Res.* **16**, 11–41.

Chen, D. & Jirka, G. H. 1997 Absolute and convective instabilities of plane turbulent wakes in a shallow water layer. *J. Fluid Mech.* **338**, 157–172.

Chen, D. & Jirka, G. H. 1998 Linear stability analysis of turbulent mixing layers and jets in shallow water layers. *J. Hydraul. Res.* **36**, 815–829.

Chen, D. & Jirka, G. H. 1999 LIF study of a plane jet bounded in shallow water layer. *ASCE J. Hydrodyn. Engng* **125**, 817–827.

Cohn, R. K. & Koochesfahani, M. M. 1993 Effect of boundary conditions on axial flow in a concentrated vortex core. *Phys. Fluids* A **5**, 280–282.

Chu, V. H. & Babarutsi, S. 1988 Confinement and bed-Friction effects in shallow turbulent mixing layers. *J. Hydraul. Engng* **114**, 1257–1274.

Chu, V. H., Wu, J.-H. & Khayat, R. E. 1991 Stability of transverse shear flows in shallow open channels. *J. Hydraul. Engng* **117**, 1370–1388.

Didden, N. 1979 On the formation of vortex rings: rolling-Up and production of circulation. *Z. Angew. Math. Phys.* **30**, pp. 101–116.

Doligalski, T. L., Smith, C. R. & Walker, J. D. A. 1994 Vortex interactions with walls. *Annu. Rev. Fluid Mech.* **26**, 573–616.

Dracos, T., Giger, M. & Jirka, G. H. 1992 Plane turbulent jets in a bounded fluid layer. *J. Fluid Mech.* **241**, 587–614.

Foss, J. F. & Jones, J. B. 1968 Secondary flow effects in a bounded rectangular jet. *Trans. ASME: J. Basic Engng*, June, 241–248.

Gharib, M., Rambod, E. & Shariff, K. 1998 A universal time scale for vortex ring formation. *J. Fluid Mech.* **360**, 121–140.

Giger, M., Dracos, T. & Jirka, G. H. 1991 Entrainment and mixing in plane turbulent jets in shallow water. *J. Hydraul. Res.* **29**, 615–641.

Grubisic, V., Smith, R. B. & Schar, C. 1995 The effect of bottom friction on shallow-flow past an isolated obstacle. *J. Atmos. Sci.* **48**, 1985–2006.

Holdeman, J. D. & Foss, J. F. 1975 The initiation, development, and decay of the secondary flow in a bounded jet. *Trans. ASME: J. Fluids Engng*, September, 342–352.

Ingram, R. G. & Chu, V. H. 1987 Flow around islands in Rupert Bay: an investigation of the bottom friction effect. *J. Geophys. Res.* **92**, (C13), 14521–14533.

Kahraman, A., Sahin, B. & Rockwell, D. 2002 Control of vortex formation from a vertical cylinder in shallow water: effect of localized roughness. *Exps. Fluids* **33**, 54–65.

Klebanoff, P. S., Tidstrom, K. D. & Sargent, L. M. 1962 The three dimensional nature of boundary layer instability. *J. Fluid Mech.* **12**, 1–24.

Koochesfahani, M. M. 1989 Vortical patterns in the wake of an oscillating airfoil. *AIAA J.* **27**, 1200–1205.

Krishnamoorthy, S. & Marshall, J. S. 1998 Three-dimensional blade–vortex interaction in the strong vortex regime. *Phys. Fluids* **10**, 2828–2837.

Kurosaka, M., Christiansen, W. H., Goodman, J. R., Tirres, L. & Wohlman, R. A. 1988 Crossflow transport induced by vortices. *AIAA J.* **26**, 1403–1407.

Lloyd, P. M. & Stansby, P. K. 1997 Shallow-water flow around model conical islands of small side slope. I: Surface piercing. *J. Hydraul. Engng* December, 1057–1067.

Marshall, J. S. & Krishnamoorthy, S. 1997 On the instantaneous cutting of a columnar vortex with non-zero axial flow. *J. Fluid Mech.* **351**, 41–74.

Perry, A. E. & Chong, M. S. 1986 A series-expansion study of the Navier–Stokes equations with applications to three-dimensional separation patterns. *J. Fluid Mech.* **173**, 207–223.

Raffel, M., Willert, C. & Kompenhans, J. 1998 *Particle Image Velocimetry: A Practical Guide.* Springer.

Rockwell, D. 1977 Vortex stretching due to shear layer instability. *Trans. ASME: J. Fluids Engng* **99**, 240–244.

Saric, W. S. & Thomas, A. S. W. 1984 Experiments on the subharmonic route to turbulence in boundary layers. In *Turbulence and Chaotic Phenomena in Fluids* (ed. T. Tatsumi), pp. 117–122. Elsevier.

Tachie, M. F. & Balachandar, R. 2001 Shallow wakes generated on smooth and rough surfaces. *Exps. Fluids* **30**, 467–474.

Uijttewaal, W. S. J. & Tucker, J. 1998 Development of quasi two-dimensional structures in a shallow free-surface mixing layer. *Exps. Fluids* **24**, 192–200.

Walker, J. D. A. 1978 The boundary layer rectilinear vortex. *Proc. R. Soc. Lond.* A **35**, 167–188.

Westerweel, J. 1993 Digital particle image velocimetry: theory and application. Doctoral Dissertation, Delft University Press.